JM PAPERS

Tomographic PIV investigation on near-wake structures of a hemisphere immersed in a laminar boundary layer

Han Tu[1,2], Zhongyi Wang[3], Qi Gao[1],†, Wenxuan She[1], Fujun Wang[1], Jinjun Wang[3] and Runjie Wei[4]

[1]State Key Laboratory of Fluid Power and Mechatronic System, School of Aeronautics and Astronautics, Zhejiang University, Hangzhou 310027, PR China

[2]Hubei Provincial Key Laboratory of Chemical Equipment Intensification and Intrinsic Safety, School of Mechanical and Electrical Engineering, Wuhan Institute of Technology, Wuhan 430205, PR China

[3]Key Laboratory of Fluid Mechanics, Ministry of Education, Beihang University, Beijing 100191, PR China

[4]MicroVec Inc., Beijing 100191, PR China

The near wake of a hemisphere immersed in a laminar boundary layer is studied utilizing time-resolved tomographic particle image velocimetry (TPIV). Focus is placed on the three-dimensional vortical structures and the formation details of hairpin vortices before the onset of transition. The three-dimensional instantaneous pressure field of the hemisphere wake is reconstructed for better understanding the flow mechanism. Experiments are carried out with Reynolds number $Re_r = 1370$, based on the hemisphere radius R. Features of periodicity of the near wake are analysed using proper orthogonal decomposition and Fourier transformation. The velocity fluctuation in the wall-normal direction is shown to be crucial to the formation of hairpin vortices in the near wake. By investigating the transport of mass and vorticity, and the correlation between pressure and hairpin vortex strength, the formation mechanism is revealed clearly. Specifically, the main hairpin vortices (MHVs) are formed within the reaction of outer high-speed flow and near-wall flow. The formation of the head portion is followed by the leg portion formation. The shedding of the MHVs is highly correlated with the pressure, as well as the pressure gradient in the wall-normal direction. For the side hairpin vortices (SHVs), the leg portion is formed first, followed by the generation of the head portion thanks to induction of the re-oriented standing vortices. The generation of the SHVs can be regarded as the downstream bridging of the standing vortices, similar to the generation of hairpin vortices due to the connection of streamwise vortices in turbulent boundary layers.

Key words: wakes

† Email address for correspondence: qigao@zju.edu.cn

1. Introduction

Investigation on vortices in turbulent boundary layers (TBLs) can give us a better understanding of the turbulent transport of mass, momentum and vorticity, which has raised a significant amount of interest in many researchers for years (Robinson 1991; Adrian, Meinhart & Tomkins 2000; Eitel-Amor *et al.* 2015). The generation and evolution of the hairpin vortices play a key role in self-sustaining the coherent structures (Adrian *et al.* 2000; Adrian 2007). However, it can be difficult to investigate hairpin vortices directly in TBLs, due to the influence of the turbulent fluctuations on the hairpin vortex evolution (Robinson 1991). The evolutionary dynamics of the coherent structures has been found to be similar in both fully turbulent and transitional shear flows (Svizher & Cohen 2006*a*). Consequently, as an alternative, studying the characteristics of hairpin vortices that are artificially generated in laminar boundary layers can reduce the complication of the investigation (Svizher & Cohen 2006*b*). Hairpin vortices can be generated manually in many ways, using an injection (Acarlar & Smith 1987*b*; Haidari & Smith 1994; Svizher & Cohen 2006*a*), a mixing tab (Pu & Meng 2000; Yang, Meng & Sheng 2001), and a smooth surface-mounted obstacle (Acarlar & Smith 1987*a*; Hajimirzaie, Wojcik & Buchholz 2012; Wood *et al.* 2016; Ye, Schrijer & Scarano 2016*a*; Belkhou *et al.* 2019; Zhang *et al.* 2021). In particular, as a prototypical smooth obstacle geometry, the surface-mounted hemisphere has been considered extensively in previous experimental and numerical studies.

As early as 1962, with the help of the vibrating-ribbon technique and hot-wire anemometry, Klebanoff, Tidstrom & Sargent (1962) found that periodic shedding vortices can be induced by a single rough hemisphere element under proper conditions. The resultant velocity profile was similar to that in the transition of a laminar boundary layer. Acarlar & Smith (1987*a*) used dye and hydrogen-bubble visualization and hot-film anemometry to investigate the structural evolution of flow structures around a hemisphere immersed in a laminar boundary layer. The flow topology can be divided roughly into: (i) a standing vortex system that forms upstream and necklaces around the hemisphere; (ii) a low-pressure recirculating region immediately downstream of the hemisphere; (iii) a main hairpin vortex (MHV) system that is formed and shed from the shear layer induced by the hemispherical obstacle; and (iv) a side hairpin vortex (SHV) system that accompanies the MHVs. Acarlar & Smith (1987*a*) concluded that the low-pressure recirculating region plays an important role in the hairpin vortex generation. The low-pressure region causes the outer flow to curve inwards and vorticity to be concentrated, which further leads to the generation of hairpin vortices. During the downstream convection of a hairpin vortex, the shear layer pushes the head portion of the hairpin to the wall, while mutual induction effects of the legs push it away from the wall. The result of these two competing mechanisms is the cancellation of vorticity in the legs of the hairpin vortex (Carr & Plesniak 2016). The mean shear flow and Biot–Savart self-induction constitute another competitive effect that affects the hairpin vortex dynamics (Hajimirzaie *et al.* 2012). Hairpin vortices tilt downstream when the former dominates, while hairpin vortices tilt upstream when the latter dominates. By investigating the formation and the shedding frequencies, Tamai, Asaeda & Tanaka (1987) found an onset of coalescence of hairpin vortices when the Reynolds number was up to a critical value of 2000. Carr & Plesniak (2016) concluded further that the hairpin vortices tend to form into groups prior to shedding for $Re_r \approx 2000$, based on the hemisphere radius R.

An immersed hemisphere subjected to a laminar boundary layer can induce laminar-to-turbulent transition. The transition process can involve different instability modes, e.g. a varicose mode and a sinuous mode (Loiseau *et al.* 2014). Tani (1981)

applied the smoke wire visualization and discussed the influence of surface humps on promoting the transition of the boundary layer and the formation of hairpin vortices. Ye, Schrijer & Scarano (2016*b*) studied the boundary layer transition behind a hemisphere, and found that the sideward low-speed regions are important for the transition. Convection and regeneration of hairpin vortices were found to be related to the sidewise propagation of the turbulent/non-turbulent interface. Ye, Schrijer & Scarano (2018) discovered symmetric and asymmetric proper orthogonal decomposition (POD) modes in the wake, which are related to the varicose mode and the sinuous mode, respectively.

At higher Reynolds numbers, i.e. in a turbulent boundary layer, hairpin-vortex-type structures can still be identified but are less coherent (Carr & Plesniak 2016). Savory & Toy (1986*b*) investigated the complex structures in the near-wake region of a hemisphere immersed in turbulent boundary layers, and gave a detailed depiction of hairpin vortices (referred as 'vortex loops') and relevant characteristic flow structures. It was found that the thickness of turbulence boundary layer and the turbulence intensity have impact on separation/reattachment of the hemispherical flow and the vortical content in the wake (Toy, Moss & Savory 1983; Savory & Toy 1986*b*; Wood *et al.* 2016). Wood *et al.* (2016) found that the shedding type differs at the lower and higher sides of the hemisphere. Consequently, a chain of entangled hairpin structures of different sizes is formed and travels downstream.

There have been many studies performed on hemispherical roughness elements (Toy *et al.* 1983; Tang & Jiang 2012; Citro *et al.* 2015), especially within turbulent boundary layers (Savory & Toy 1986*b*; Manhart 1998; Tavakol & Yaghoubi 2010; Tavakol, Yaghoubi & Motlagh 2010; Guala *et al.* 2012; Wood *et al.* 2016; Cao & Tamura 2020; Li *et al.* 2022). Previous investigations also include particle transport in hemispherical wakes (Prevel *et al.* 2013; Gao *et al.* 2021), hemisphere in pulsatile flows (Carr & Plesniak 2016; Carr *et al.* 2020), and hemispherical wakes in the supersonic regime (Wang *et al.* 2012; Mortazavi *et al.* 2014; Kiriakos *et al.* 2021). Large-eddy simulations (LES) and direct numerical simulations (DNS) have been applied widely in the above-mentioned studies. For experimental investigations, dye/bubble visualization has been used extensively. Planar particle image velocimetry (PIV) and stereoscopic PIV also have been used to measure the velocity in typical cross-sections or the time-averaged flow field behind a hemisphere. Many characteristics of hemispherical wakes and important structures in typical cross-sections (e.g. the symmetric plane) have been revealed. However, relevant investigations with the time-resolved three-dimensional (3-D) experimental measurements are limited, and studies of comprehensive analysis based on both kinematic and dynamic (e.g. pressure) perspectives are barely seen in the literature. In addition, the flow around an isolated obstacle immersed in a laminar and incompressible developing boundary layer has been relatively less reported in the literature (Belkhou *et al.* 2019). Consequently, insight into related coherent structures may be insufficient (Johnson *et al.* 2017), and previous understandings of the 3-D characteristics, generation and evolution of the hairpin vortices may be incomplete. Notably, compared to the MHVs, the SHVs receive much less attention, leading to a lack of observation and explicit explanation of generation mechanism. There are different views on the SHV formation: Savory & Toy (1986*a*) pointed out that vortices in the SHV region curl around each other as they move downstream; Acarlar & Smith (1987*a*) found that the generation of the SHVs appears to be due to the interaction between the flow induced by the standing vortices and the higher-speed outer boundary layer flow; Ye *et al.* (2016*b*) observed that the SHVs are generated bounding the MHVs. The current study employs tomographic particle image velocimetry (TPIV) and 3-D pressure reconstruction for a quantitative investigation of the

near-wake structures. The evolution processes and formation mechanisms of the MHVs and SHVs are evidenced clearly based on the current measurements.

The TPIV technique developed by Elsinga *et al.* (2006) is the most widely used technique for 3-D velocity measurement to date. With the multiplicative algebraic reconstruction technique (MART), it realizes the flow measurement with high spatial resolution and accuracy. The TPIV technique has been demonstrated as an effective tool for complex 3-D flow measurements (Gao, Wang & Shen 2013; Scarano 2013), such as the cylinder wake (Zhu *et al.* 2017; Rinoshika *et al.* 2021), wakes of stationary and freely moving spheres (van Hout *et al.* 2018, 2022; Eshbal *et al.* 2019), near-wall turbulence (Schröder *et al.* 2008; Gao, Ortiz-Dueñas & Longmire 2011; Wang *et al.* 2019) and wakes of aquatic organisms (Adhikari & Longmire 2013; Murphy *et al.* 2016; Mohaghar, Adhikari & Webster 2019; Tu *et al.* 2022). With the access of time-resolved 3-D velocity data, 3-D pressure reconstruction with high spatial and temporal resolution has become achievable. Generally, two steps are necessary to reconstruct pressure from time-resolved velocity data. The first step is to calculate the pressure gradient terms from velocity fields. The viscous term in the Navier–Stokes equations is normally ignored since it is usually negligible compared with other terms (Thomas & Liu 2004; van Oudheusden *et al.* 2007; Koschatzky *et al.* 2011). Therefore, the calculation of material acceleration becomes the most important task for the pressure reconstruction (Lynch & Scarano 2013). The second step is to integrate the pressure gradient (de Kat & Ganapathisubramani 2013; Liu & Katz 2013; Wang *et al.* 2016*d*) or solve the Navier–Stokes equations directly (Wang *et al.* 2017*a*) to obtain the pressure field. By applying physical constraints (e.g. the Navier–Stokes equations; Wang *et al.* 2016*d*, 2018) or schlieren image (Cai *et al.* 2021), the pressure reconstruction error can be reduced further. There have been numerous studies that reported on the pressure reconstruction based on PIV (Gresho & Sani 1987; Baur 1999; Gurka *et al.* 1999; Christensen & Adrian 2002; Liu & Katz 2006, 2013; Novara & Scarano 2012*b*; Dabiri *et al.* 2014). Both numerical and experimental applications have proved the effectiveness and validity of this technique (van Oudheusden 2013).

In the current work, the near-wake structures of a hemisphere immersed in a laminar boundary layer are measured using time-resolved TPIV. As far as the authors are aware, no time-resolved 3-D measurements have been reported in the literature to reveal detailed formation processes of the MHVs and SHVs, or to investigate quantitatively the generation mechanism of the latter. The main intention of the current work is to fill the aforementioned gap and attempt to improve the current conceptual model of hairpin vortex formation. Similarities and differences in the formation processes and mechanisms of hairpin vortices in the hemisphere wake are to be discussed. For this objective, flow characteristics, including the time-averaged flow pattern, fluctuation, periodicity of the flow, transport of mass and vorticity, and pressure distribution, are analysed. Mechanisms driving the formation and evolution of the hairpin vortices are investigated from both the kinematic and dynamic perspectives.

This paper is constructed as follows. In § 2, detailed information on the experimental set-up and TPIV measurements is described. Section 3 presents the basic mean flow field and statistics of the near wake. In § 4, a POD analysis for the near wake is performed. The periodicity of the flow is investigated, and transport of mass and vorticity during the formation of hairpin vortices is analysed. Accordingly, new sketches of the formation mechanisms of the MHVs and SHVs are obtained in §§ 4.2 and 4.3, respectively. We end the paper with conclusions in § 5.
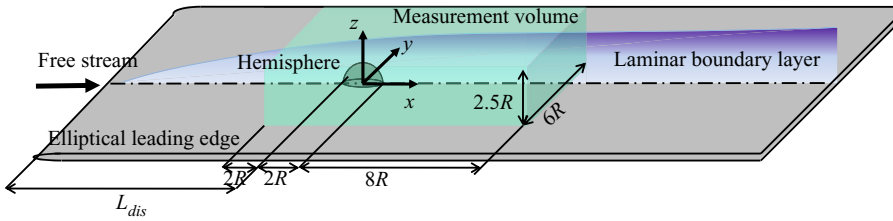
Figure 1. Schematic of the experiment model and the coordinate system.

2. Experimental set-up and measurement technique

2.1. *Experimental set-up*

All experiments were conducted in a low-speed circular open water channel in Beihang University, China. The dimensions of the test section are 3000 mm × 600 mm × 700 mm in the streamwise, spanwise and vertical directions, respectively. The turbulence intensity is less than 0.8 % at the free-stream velocity (145.27 mm s^{-1}) used for the TPIV measurements.

Figure 1 gives a schematic of the experimental model and the coordinate system. The hemisphere was fixed on a flat plate, and the profile of the front edge is semi-elliptical with the ratio of the long to the short axis being 4 : 1. A laminar boundary layer was developed along the flat plate. See Appendix A for validation of the undisturbed boundary layer profile. Previous studies on the same facility have demonstrated the stable behaviour of the boundary layer, i.e. no leading edge separation exists, and the zero-pressure-gradient condition is well maintained (Pan *et al.* 2008; He, Wang & Pan 2013; Deng, Pan & Wang 2014). The orientations of the (x, y, z) Cartesian coordinate system defined herein correspond to the streamwise direction, the spanwise direction and the wall-normal direction of the flat plate, respectively. And the coordinate origin is located at the centre of the circle, which is the contact surface between the tested hemisphere and the flat plate. Note that the flat plate was placed vertically in the channel rather than horizontally, for the ease of the construction of the experimental platform. Therefore, the y axis and the z axis correspond to the vertical direction and the spanwise direction of the channel, respectively. As a characteristic length, the radius R of the hemisphere is 10 mm. The geometry of the flat plate in three directions (x, y, z) is $200R \times 50R \times R$ (2000 mm × 500 mm × 10 mm). In addition, the distance from the leading edge of the hemisphere to the leading edge of the plate is $L_{dis} = 70R$ (700 mm), and the size of the measurement volume is $12R \times 6R \times 2.5R$ (120 mm × 60 mm × 25 mm).

The Reynolds number based on the hemisphere radius is 1370 ($Re_r = U_\infty R/\nu$, where ν is the kinematic viscosity of the fluid), and the Reynolds number at the height of the hemisphere is 1332 ($Re_h = u_h R/\nu$, where u_h is the undisturbed velocity at height $h = 10$ mm). The critical Reynolds number, which scales with $(h/c)^{2/5}$ (Townsend 1961, height-to-span ratio), ranges from 455 to 682 for the tested hemisphere. Therefore, the current experiments were conducted in the supercritical regime. The undisturbed laminar boundary layer thickness θ is 11.65 mm, and the ratio of boundary layer thickness and hemisphere radius (δ/R) is 1.165, resulting in the hemisphere being fully immersed in the laminar boundary layer. The laminar flow regime in the boundary layer is indicated by the measured shape factor ($H = 2.59$). Relevant properties of the boundary layer, including displacement thickness (δ^*) and momentum thickness (θ), are summarized in table 1. It is also necessary to note the symbol definitions of the current work: u, v and w denote the

U_∞ (mm s^{-1})	δ (mm)	δ^* (mm)	θ (mm)	H	Re_r	Re_h	δ/R
145.27	11.65	3.89	1.50	2.59	1370	1332	1.165

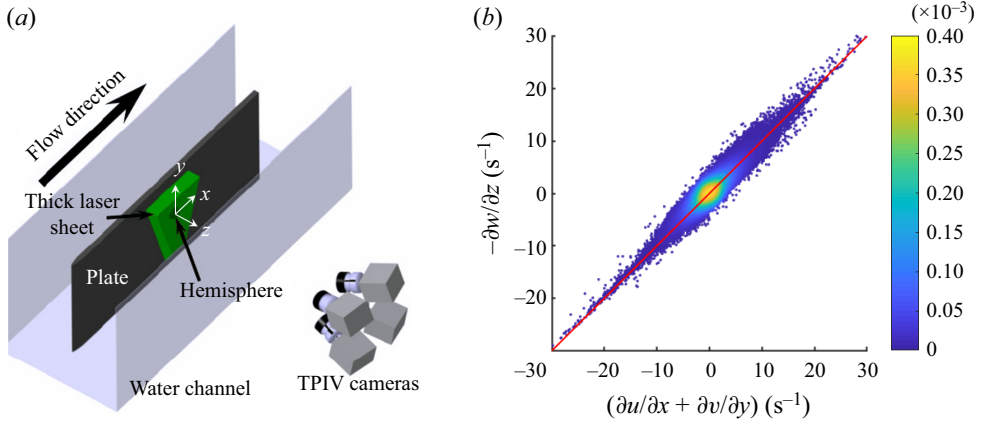Table 1. Incoming flow conditions and boundary layer integral parameters.

Figure 2. (*a*) Experimental set-up for TPIV measurements; the origin of the coordinate system is at the centre of the hemisphere bottom surface. (*b*) Joint probability density function of $(\partial u/\partial x + \partial v/\partial y)$ and $-\partial w/\partial z$ evaluated in planes $y/R = 0$ and $y/R = -1.6$.

instantaneous streamwise, spanwise and wall-normal velocity components, respectively; velocity fluctuations are denoted by a prime; an overbar indicates temporal averaging, and an angle bracket $\langle \ldots \rangle$ indicates root-mean-square (r.m.s.) calculating.

2.2. *Time-resolved TPIV*

A high-speed TPIV system was built to measure the time-resolved 3-D velocity fields of the hemisphere wake. The TPIV arrangement is shown in figure 2(*a*). Tracers of the TPIV measurements were glass hollow particles with diameter approximately 10 μm and density 1.05 g cm^{-3}. The particle seeding density was approximately 0.05 particles per pixel. Illumination was provided by a Vlite-Hi-527-30 high-frequency laser (Nd:YLF, 2×30 mJ pulse^{-1} at 1 kHz, Beamtech., Inc.). The wavelength of the laser was 527 nm. The optical lens and mirrors (two cylindrical convex mirrors, one planar mirror and one cylindrical concave mirror) were arranged to generate a 25 mm thick light sheet illuminating the particles around the tested hemisphere. The light sheet was parallel to the flat plate, and a reflecting mirror was mounted to reduce the shadow. The tested hemisphere was fully included in the light sheet. The imaging system consisted of 4 Fastcam Photron SA2 CMOS cameras, which were fixed in a cross-like arrangement from one side of the channel. The resolution of the cameras was set to 2048×1024 pixels to achieve imaging in conjunction with the rectangular-shaped measurement area. Each camera was equipped with an 85 mm Nikon lens with aperture $f_\# = 11$, and the Scheimpflug angle was adjusted. The view angles between the two neighbouring cameras were approximately 30°. The cameras and the high-frequency laser were synchronized and controlled by a Micropulse 725 synchronizer from MicroVec., Inc. The sampling frequency for this measurement

was 250 Hz. Since the frequency of vortex shedding was 6.8 Hz at Reynolds number $Re_r = 1370$, the sampling frequency 250 Hz can resolve the periodic flow structures. To ensure that the dataset has a sufficient temporal length for further statistical analysis, and to take into account the high computational cost of TPIV processing, 1250 frames were processed.

The PIV software MicroVec4 v1.1 (MicroVec., Inc.) was used for TPIV data acquisition and processing. The volume calibration of the tomographic image and the self-calibration procedure (Wieneke 2008) were performed to reduce the disparity error of the original mapping functions to be less than 0.1 pixels, corresponding to 1.1 % of the free-stream velocity U_∞. The intensity-enhanced multiplicative algebraic reconstruction technique (IntE-MART) algorithm, the dual-basis pursuit algorithm and volume-deformed 3-D correlation analysis with multi-passes were applied to the particle reconstruction and the correlation analysis (Ye *et al.* 2015; Wang *et al.* 2016c). The corresponding 3-D reconstruction volume had dimensions 110 mm $\times$ 46 mm $\times$ 20 mm ($11R \times 4.6R \times 2R$ in the streamwise, spanwise and vertical directions). The magnification was 0.064 mm pixel^{-1}. The 3-D velocity fields were evaluated with a multi-grid interrogation scheme with final interrogation volume size $48 \times 48 \times 48$ pixels and overlap rate 75 %. The reconstructed velocity fields were distributed on a $143 \times 59 \times 25$ spatial grid with vector spacing 0.768 mm. And the velocity fields were further post-processed by a robust divergence-free smoothing algorithm (Wang *et al.* 2016a) to remove the potential outliers and reduce noise.

The experimental uncertainty is an important issue for PIV experiments to evaluate the quality of the measurement. For the reconstruction and cross-correlation procedure, a typical uncertainty value 0.3 voxels in the instantaneous velocity field is considered (Lynch & Scarano 2015). The uncertainty in the mean flow depends on the number of samples N_s and the typical level of streamwise velocity fluctuations σ_u. In the current study, the dataset contains 250 snapshots with PIV cross-correlation independence, and $\langle u' \rangle / U_\infty$ is approximately 0.15. The normalized uncertainty in the mean field could be estimated by $\varepsilon_u / U_\infty = \sigma_u / \sqrt{N_s} \approx 0.0095$. Similarly, the normalized uncertainty in the r.m.s. of the velocity fluctuation is estimated by $\varepsilon_{u'} / U_\infty = \sigma_u / \sqrt{(2N_s - 1)} \approx 0.0067$. For an incompressible flow like the present hemisphere wake, the divergence of the velocity is required to be identically zero by the conservation of mass, namely

$$\nabla \cdot \boldsymbol{u} = \frac{\partial u}{\partial x} + \frac{\partial v}{\partial y} + \frac{\partial w}{\partial z} = 0. \tag{2.1}$$

Following the paradigm of Jodai & Elsinga (2016); van Hout *et al.* (2018), the joint probability density function (p.d.f.) of $(\partial u / \partial x + \partial v / \partial y)$ and $-\partial w / \partial z$ for data points in planes $y/R = 0$ and $y/R = -1.6$ within 100 consecutive frames is shown in figure 2(b). The joint p.d.f. should collapse onto the red diagonal if the continuity equation is satisfied perfectly. Data points away from the red diagonal correspond to non-zero divergence, thus indicating measurement error. As shown in figure 2(b), the joint p.d.f. of the dataset represents an elongated ellipse, and the corresponding R^2 value is higher than 0.85, ensuring that the residuals of the continuity equation are maintained to a small extent.

2.3. *Proper orthogonal decomposition*

Proper orthogonal decomposition (Lumley 1967, POD) is an effective modal analysis method, which decomposes the velocity fluctuation into a series of orthogonal modes

$\varphi_n(x, y, z)$ and corresponding time-dependent amplitude coefficients $\alpha_n(t)$ as follows:

$$u'(x, y, z, t) = \sum_{n=1}^{N} \alpha_n(t)\, \varphi_n(x, y, z), \qquad (2.2)$$

where N is the number of orthogonal modes. The modes are sorted in descending order of energy, so that the first several modes occupy a larger percentage of the total energy, thereby extracting the main features of the flow. Since it can extract efficiently the main characteristics and coherent structures of the flow field, POD has been applied widely as a data reduction approach for TPIV experiments by past works (Wang *et al.* 2016*b*; Zhu *et al.* 2017; Ye *et al.* 2018). The snapshot POD method (Sirovich 1987) was applied to the current TPIV experimental investigation.

2.4. *PIV-based pressure reconstruction*

The pressure field is significant in the study of dynamic characteristics in fluid mechanics. To reveal the major characteristics of the pressure evolution and filter out small-scale structures, the instantaneous pressure fields were reconstructed from velocity fields that consist of POD modes occupying the top 50 % of the total energy. Then the time-averaged pressure field was obtained by averaging instantaneous pressure snapshots. The processing of this reconstruction is usually divided into two steps: first, the pressure gradient distribution is obtained through the velocity terms of the Navier–Stokes equations; second, the pressure field is reconstructed from the pressure gradient using a certain integration scheme. A brief introduction to pressure reconstruction and relevant techniques is given below.

The incompressible Navier–Stokes equation can be written as

$$\nabla p = -\rho\, \frac{\mathrm{D}\boldsymbol{u}}{\mathrm{D}t} + \mu\, \nabla^2 \boldsymbol{u}, \qquad (2.3)$$

where ∇p is the pressure gradient, ρ is the density, $\mathrm{D}\boldsymbol{u}/\mathrm{D}t$ is the material acceleration, and $\mu\, \nabla^2 \boldsymbol{u}$ is the viscous term. For the flow with a high Reynolds number, the viscous term is normally at least two orders smaller than the material acceleration term (Thomas & Liu 2004; van Oudheusden 2008; Koschatzky *et al.* 2011). Based on the current measurements, the magnitude of the acceleration term is approximately $\sim 10^3$ times that of the viscous term. The viscous term is definitely a small quantity compared to the acceleration. Therefore, the contribution of the viscous term to the pressure gradient is omitted. In other words, only the material derivative term $\mathrm{D}\boldsymbol{u}/\mathrm{D}t$ is used to obtain the pressure gradient ∇p.

The material derivative term can be calculated from either an Eulerian approach or a Lagrangian approach. In this work, we adopted an imaginary particle tracking accelerometry (IPTA; Wang *et al.* 2017*b*), which is a novel Lagrangian approach, to evaluate the material acceleration. The material derivative term can be obtained by tracing virtual particles using the equation (Novara & Scarano 2012*a*):

$$\frac{\mathrm{D}\boldsymbol{u}}{\mathrm{D}t} = \frac{\mathrm{d}\boldsymbol{u}_p(t)}{\mathrm{d}t} = \frac{\mathrm{d}\boldsymbol{u}(\boldsymbol{x}_p(t), t)}{\mathrm{d}t}, \qquad (2.4)$$

where $\boldsymbol{x}_p(t)$ and $\boldsymbol{u}_p(t)$ are the position and velocity of the traced virtual particle at time t, respectively. Traced objects can be real seeding particles/particle clusters or virtual

particles initiated from velocity fields. Equation (2.4) can be discretized as

$$\left.\frac{\mathrm{D}\boldsymbol{u}}{\mathrm{D}t}\right|_{\boldsymbol{x}_a+\boldsymbol{u}_a\,\Delta t/2,\,t+\Delta t/2} = \frac{\boldsymbol{u}_2(\boldsymbol{x}_a+\boldsymbol{u}_a\,\Delta t,\,t+\Delta t) - \boldsymbol{u}_1(\boldsymbol{x}_a,\,t)}{\Delta t}, \tag{2.5}$$

where Δt is the temporal step, $\boldsymbol{u}_1$ and $\boldsymbol{u}_2$ are the velocities of the traced virtual particle at t and $t + \Delta t$, respectively, and $\boldsymbol{u}_a$ is the averaged Lagrangian velocity of the particle, which can be obtained by an iterative approach. According to de Kat & van Oudheusden (2012), the uncertainty of the material acceleration computation with the Lagrangian approach is evaluated as $\varepsilon_{\mathrm{D}\boldsymbol{u}/\mathrm{D}t}^2 \approx \varepsilon_u^2(1/(2\,\Delta t^2) + \frac{1}{2}\,|\boldsymbol{\nabla}\boldsymbol{u}|^2) \approx 0.09 \ \mathrm{m}^2\ \mathrm{s}^{-4}$. As a sophisticated Lagrangian approach, IPTA suppresses the uncertainty to a lower extent. Further details can be found in Wang *et al.* (2017*b*).

After evaluating the material acceleration, namely the pressure gradient, an irrotation correction scheme is applied on the pressure gradient to further suppress errors, and an orthogonal-path integration scheme is utilized to reconstruct the pressure field. The accuracy, uncertainty and further details can be found in Wang *et al.* (2016*d*). Based on the pressure $p(s_{ref})$ at the reference location, the pressure $p(s_{tar})$ at the target location is calculated by selecting the integral path for spatial eroding integration (Discetti, Natale & Astarita 2013), given by

$$p(s_{tar}) = p(s_{ref}) + \int_{s_{ref}}^{s_{tar}} \boldsymbol{\nabla}p \cdot \mathrm{d}\boldsymbol{s}, \tag{2.6}$$

where $\boldsymbol{s}$ is the integration variable of the particle location. With the above procedures, the instantaneous pressure fields are reconstructed eventually. Note that all pressure fields presented in the current study are not absolute pressures, but relative pressures. Limited by the size of the measurement domain, the reference pressure point ($p_0 = 0$) cannot be selected at an area that is far enough from the hemisphere. In line with Qin & Meng (2009), the reference pressure point is set at the first grid point next to the intersection of the wall and the trailing edge of the hemisphere in the recirculation region. Since the pressure fluctuation is relatively minor in the recirculation region, the location at the intersection of the trailing edge and the flat plate is considered a favourable choice of the reference point.

3. Statistics of the flow field

3.1. *Basic mean flow field*

The basic mean flow field, which is obtained by averaging over 1250 instantaneous TPIV snapshots at $Re_r = 1370$, around the hemisphere presents apparent characteristics of complex 3-D separation. Figure 3 gives the time-averaged dimensionless streamwise velocity contours and in-plane mean streamlines in the cross-sections of $y/R = 0$ and $z/R = 0.16$. Induced by the standing vortices, the flow convects to the flat plate before the stagnation point, which is indicated by the downward curved streamlines at the leading edge of the hemisphere, as shown in figure 3(*a*). The flow is separated at the top of the hemisphere, and a large recirculation region appears downstream. Around $x/R = 2.75$, a spiral point (labelled 'SP') is detected, which hints the existence of a clockwise-rotating vortex. Due to the induction of the clockwise-rotating vortex and the entrainment of fluid from the sides, the streamlines in the recirculation region point upwards to the separated shear layer. This leads to an increase of the boundary layer thickness in the range $0 < x/R < 2.85$. Slightly downstream, a saddle point (labelled 'S') is captured, which is a byproduct of the downwash effect and the streamwise acceleration in the wake at $x/R = 3$.
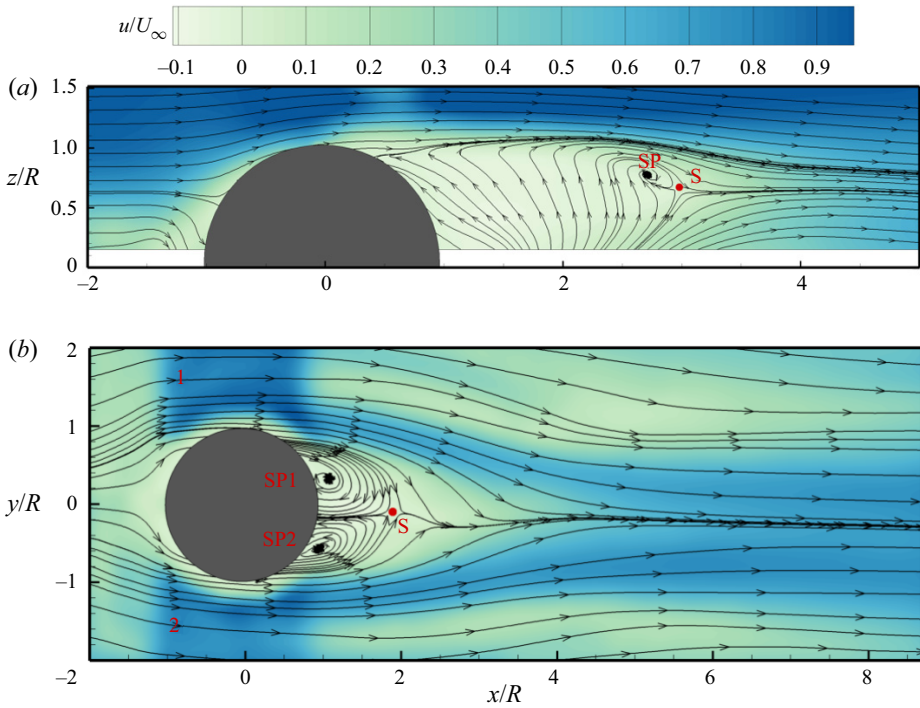
Figure 3. Distribution of time-averaged dimensionless streamwise velocity and mean streamlines: (a) constant-spanwise cut $y/R = 0$; (b) constant wall-normal cut $z/R = 0.16$.

Figure 3(b) depicts the distribution of time-averaged dimensionless streamwise velocity and mean streamlines in the $z/R = 0.16$ plane. Note that the distribution is not perfectly symmetric about $y/R = 0$. Since the alignment of the coordinate system with the streamwise direction was checked, this asymmetry is most likely due to the influence of gravity as the set-up was placed vertically (see figure 2a). Two spiral points (labelled 'SP1' and 'SP2') and a saddle point (labelled 'S') are apparently revealed by the mean streamlines. SP1 and SP2 hint at the recirculating effect in the near wake, and saddle S indicates the closure of the separation region. Two distinct high streamwise velocity regions (labelled '1' and '2') appear on each side of the hemisphere, due mainly to the re-orientation of the standing vortices and the acceleration effect, which are caused by the obstacle effect of the hemisphere. In the wake of the hemisphere, low- and high-streamwise-velocity regions occur alternately along the y direction, and the flow evolves gradually into a quasi-parallel structure, which is similar to previous observation downstream of a roughness element (Ye *et al.* 2016b; Zhang *et al.* 2021).

Figure 4(a) shows the distributions of time-averaged dimensionless streamwise vorticity in the planes $x/R = -1, 2, 5, 8$. The upstream dominant flow structures are composed of the standing vortices PSV1, SSV1 and PSV2. Details of the standing vortex system are given in Appendix B. Downstream of the hemisphere, a pair of counter-rotating mean streamwise vortices can be observed in the immediate wake ($-1 < y/R < 1$), which are commonly referred to as base vortices (BVs; Hajimirzaie *et al.* 2012; Zhang *et al.* 2021). The downstream re-oriented PSV1 and SSV1 are consistent with streamwise vortices that have been documented for wall-mounted obstacles (Savory & Toy 1986a; Zhang *et al.* 2021). The base vortices and re-oriented standing vortices are the major characteristics
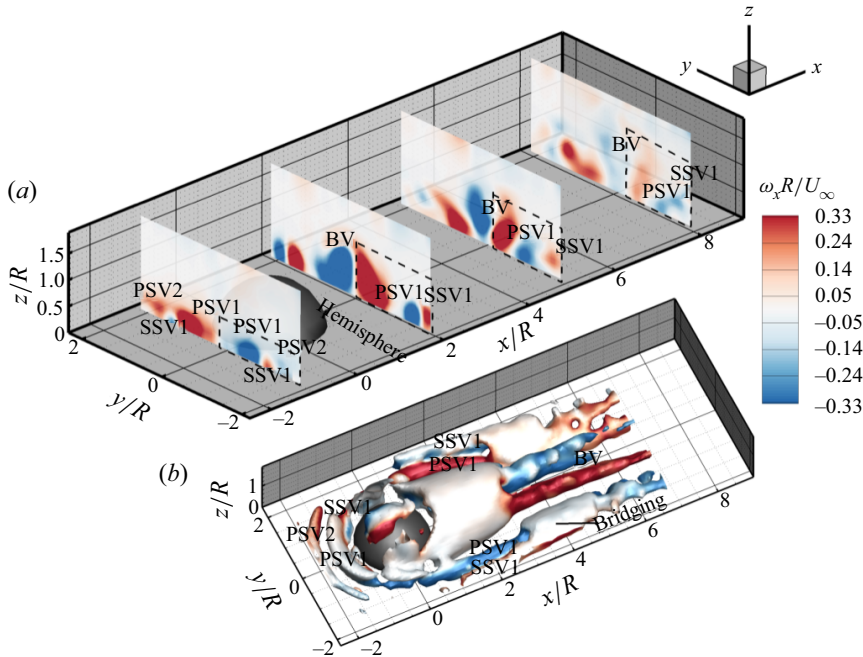
971 A36-10

Figure 4. Time-averaged (*a*) dimensionless streamwise vorticity distributions in the $x/R = -1, 2, 5, 8$ planes, and (*b*) λ_{ci} isosurface superimposed with dimensionless streamwise vorticity contours.

of the downstream flow field. Note that PSV2 is not captured downstream due to the limitation on the width of the measurement field. As indicated by the rising and fading of blue and red contours in the spanwise cross-sections, the wall-normal position of the base vortex pair continues to increase when convecting downstream, while its vortical strength decreases gradually due to the viscous dissipation. The wall-normal position of PSV1 also increases slowly during downstream convection. Compared with the slight rise of PSV1, the wall-normal position of SSV1 increases quickly from a location lower than PSV1 at $x/R = -1$ to a significantly higher location at $x/R = 8$.

Figure 4(*b*) shows λ_{ci} (Zhou *et al.* 1999) isosurfaces with threshold $\lambda_{ci} = 0.4\lambda_{ci,max}$, and dimensionless streamwise vorticity contours that are superimposed on the isosurfaces. Downstream of the hemisphere, the curved light isosurface indicates the separated shear layer. Further downstream, two slender isosurfaces, superimposed with blue and red contours, correspond to the base vortices. In addition, the standing vortices are captured clearly by the bent tubular isosurfaces in front of the hemisphere and streamwise isosurfaces in the wake. These aforementioned counter-rotating streamwise vortices transport the high-speed fluid from higher wall-normal positions towards the wall, and the low-speed fluid is transported away from the wall (Cherubini *et al.* 2013), resulting in low/high streamwise velocity regions observed in figure 3(*b*). It is worth noting that PSV1 and SSV1 tend to bridge around $x/R = 3.5$, actually revealing the formation of the SHVs from the time-averaged perspective. Details of the SHV formation will be presented in § 4.3, which fulfils the quantitative investigation of the hemisphere near wake and further indicates a more specific formation mechanism of the SHVs compared with previous studies.

The corresponding time-averaged pressure field is given in figure 5. As indicated by blue contours downstream of the hemisphere, a low-pressure region can be observed
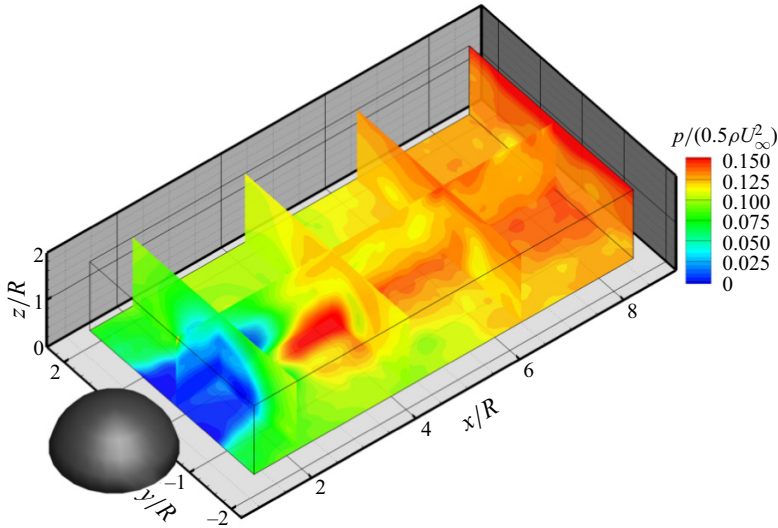
Figure 5. Time-averaged dimensionless pressure distributions in representative spanwise and vertical cross-sections.

in the near wake, which causes directly the formation of the recirculation region and the onset of the downwash effect in this region. The reconstructed pressure distribution confirms that the formation mechanism of the MHVs is the reaction of the outer flow to the low-pressure region (Acarlar & Smith 1987*a*). Downstream of the recirculation region, the pressure is recovered rapidly, which results in a high-pressure zone and further creates an adverse pressure gradient from the point of view of the time-averaged pressure field. An adverse pressure gradient is the dynamic causation of many unsteady flow patterns (e.g. separation over an aerofoil at a large angle of attack). In the current time-averaged scenario, the high local pressure gradient would imply significant events in the MHV evolution, such as shedding. Later, in § 4.1, we will show that the vortical strength of the hairpin vortices is highly correlated with the pressure, and the variation of pressure is one of the important reasons for the MHV formation and shedding. Downstream of the shedding position, the magnitude of streamwise pressure gradient is reduced. However, the overall pressure field tends to have a higher value close to the wall. Such a pressure distribution gives an explanation for the existence of the lifting-up flow ejections near the wall (see figure 3*a*), from a dynamic point of view. In the spanwise cross-sections, low-pressure regions close to the central plane of the measurement volume ($y/R = 0$) are visualized clearly by green/yellow contours, which denote the base vortices through the section. Between the base vortices (closer to the central plane), the pressure has a higher value near the wall. On the outside of the base vortex pair, the pressure increases along the positive z direction. This pressure distribution is consistent with the rotating directions of the base vortices.

3.2. *Velocity statistics*

To investigate the momentum deficit and properties of the shear layer in the near wake, the time-averaged dimensionless streamwise velocity profiles in the $y/R = 0$ central plane at different streamwise locations are obtained and shown in figure 6. The red solid dots represent the undisturbed boundary layer profile measured by planar PIV. Recall that this
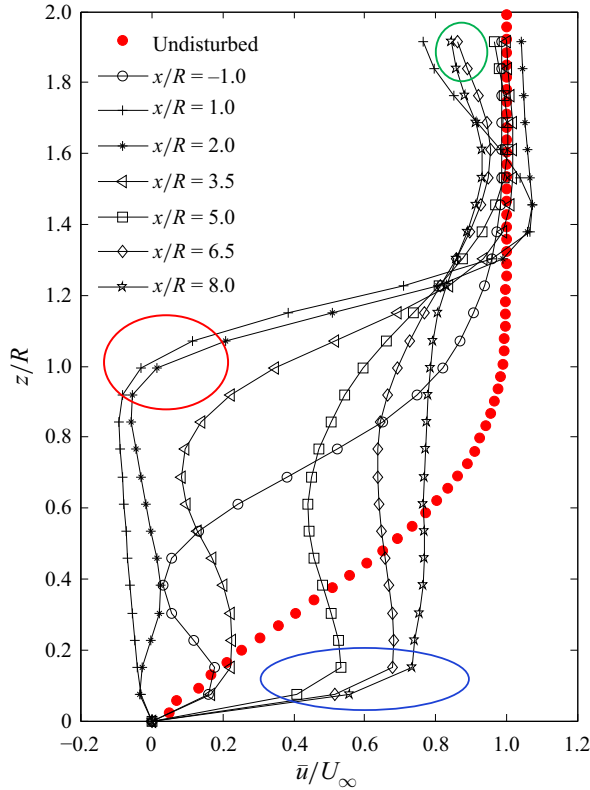
971 A36-12

Figure 6. Velocity profiles at different streamwise locations and the undisturbed velocity profile without the hemisphere (red dotted line). Featured behaviours are highlighted by ellipses of different colours.

profile agrees well with the Blasius solution. At $x/R = -1$, the streamwise velocity is reduced to zero in the range $0.1 \leq z/R \leq 0.4$, which is associated with the spanwise rotation of the standing vortices. At $x/R = 1$ and $x/R = 2$, the streamwise velocity is basically negative below $z/R = 1$, which is related to the recirculation region shown in figure 3(a). As highlighted by the red ellipse, the streamwise velocity increases quickly above $z/R = 1$, resulting in a high velocity gradient in the near wake. This again reveals the presence of a strong shear layer on the top of the hemisphere. The velocity profiles at $x/R = 5$ to $x/R = 8$ have similarities with each other: the streamwise velocity increases quickly to a moderate magnitude (highlighted by the blue ellipse) and then approaches the free-stream speed. In this range, the counter-rotating legs of the MHVs entrain nearby fluid into the central plane, which causes the increase of the local streamwise velocity. Apparently, the velocity profile at $x/R = 3.5$ is the transition between profiles in the ranges $x/R = 1$–2 and $x/R = 5$–8, since incomplete MHVs exist in this location. Basically, the streamwise velocity reaches the free-stream speed above $z/R = 1.2$, which indicates that the thickness of the boundary layer is increased due to the shear layer separation and the hairpin vortices. As highlighted by the green ellipse, the velocity profiles at $x/R = 6.5$ and 8 never reach the free-stream speed, because the MHVs have a convection velocity lower than U_∞. Briefly, the momentum deficit induced by the hemisphere is highly correlated with the formation and convection of the MHVs. Similar to the observation of the micro-ramp wake (Ye *et al.* 2016a), the wake recovery in the current study is dominated by the hairpin vortices.
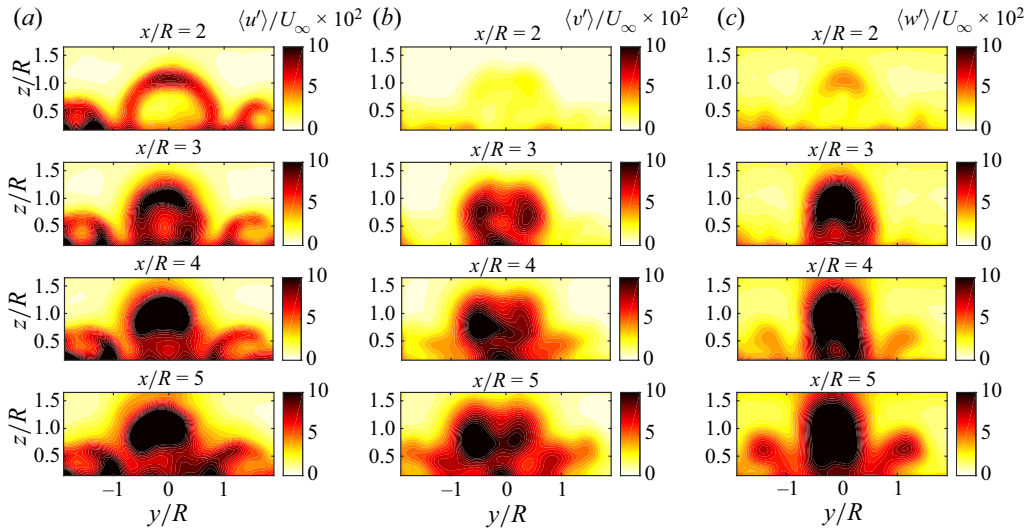
Figure 7. The r.m.s. fluctuations of velocity components in planes $x/R = 2, 3, 4, 5$.

Figure 7 gives the r.m.s. values of velocity fluctuations in cross-sections at different streamwise locations ($x/R = 2, 3, 4, 5$). In the very near wake ($x/R = 2$), the distribution of high fluctuations in u (figure 7a) features three arc-like shapes. The larger one corresponds to the shear layer separating the low-speed region from the outer flow. The two smaller arc-like shapes on both sides bound the streamwise re-oriented standing vortices. Compared with the fluctuations in the u component, fluctuations in v (figure 7b) are much weaker in the very near wake, indicating that no significant spanwise transport exists before the formation of the MHVs and the SHVs. Conversely, relatively strong fluctuations in w can be observed at the top of the shear layer and both sides of the hemisphere, which may be relevant to the downwash effect in the recirculation region and lifting-up flows induced by the streamwise standing vortices, respectively. Though later (in § 4.1) it will be shown that the wall-normal velocity fluctuations with a pulsatile mode are important for the formation of the hairpin vortices, the very near wake is dominated by the streamwise fluctuations. Further downstream ($x/R > 3$), with the generation of the MHVs and SHVs, fluctuations in v and w intensify and are comparable to the streamwise fluctuations.

To study the momentum exchange caused by velocity fluctuations in the near wake, Reynolds stress term $\overline{u'w'}/U_\infty^2$ is calculated and shown in figure 8. In the central plane of the MHVs ($y/R = 0$), negative Reynolds stress (blue contours) in the area of the MHV head portion indicates strong ejection and sweeping (Corino & Brodkey 1969) momentum transport between the outer flow and the near wall flow. Positive Reynolds stress (red contours) exists obliquely below the negative Reynolds stress area, which is similar to the observation of Gao *et al.* (2021). Recall in figure 6, the velocity profile exhibits a 'concave' shape in the range $0.4 < z/R < 1$ due to the velocity deficit in the near wake. Therefore, u' and w' with the same sign are more likely to be associated with each other, resulting in the presence of positive $\overline{u'w'}/U_\infty^2$ in the recirculation region. In the central plane of one side SHVs ($y/R = -1.6$), negative Reynolds stress also indicates ejection and sweeping momentum transport in the area of the SHV head portion. Different from figure 8(*a*), no strong positive Reynolds stress exists beneath the negative Reynolds stress area, since the SHVs are formed outside of the recirculation region. The other two

971 A36-14

(*a*)

$y/R = 0$ $\qquad \overline{u'w'}/U_\infty^2 \times 10^3$

(*b*)

$y/R = -1.6$ $\qquad \overline{u'w'}/U_\infty^2 \times 10^3$
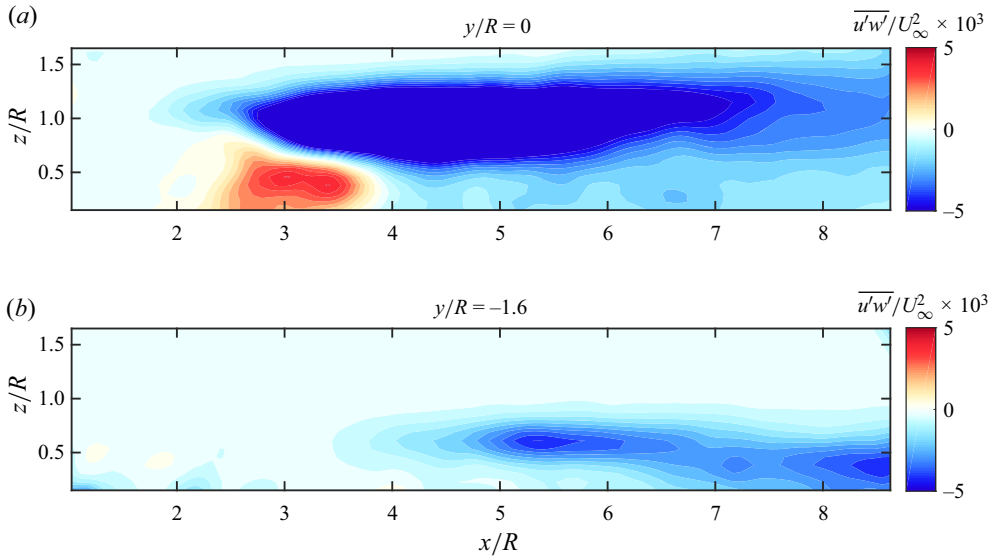
x/R

Figure 8. Distributions of Reynolds shear stress in the central planes of (*a*) MHV and (*b*) SHV region.

Reynolds shear stresses, which reveal momentum transport in the *x–y* and *y–z* orientations, have magnitudes smaller than that of $\overline{u'w'}/U_\infty^2$. For brevity, results of other Reynolds stress terms are not presented here.

The production of turbulent kinetic energy is examined to characterize the source of velocity fluctuations. The production term P follows the turbulent kinetic energy budget (Kundu, Cohen & Dowling 2015) as

$$P = -\overline{u'_i u'_j} \frac{\partial \overline{u_i}}{\partial x_j}. \qquad (3.1)$$

Figure 9 shows the normalized production term in cross-sections at different streamwise locations ($x/R = 2, 3, 4, 5$). In-plane time-averaged velocity vectors are added to ease the interpretation of results. Though strong shear motions are expected in the very near wake ($x/R = 2$), Reynolds stress terms with low magnitudes prevent more energy being extracted from the mean flow. The contribution of turbulence production to velocity fluctuations is limited in this region. At $x/R = 3$, a maximum of production is observed in the region dominated by the MHVs. Further downstream ($x/R > 3$), the strength of turbulent production intensifies in the region of SHVs, while the production strength located in the MHVs region decreases. The latter is ascribed to the wake recovery process. Recall the downstream intensification of the velocity fluctuations (figure 7): the hairpin vortices are active in transferring mean flow kinetic energy into turbulence.

4. Coherent structures and formation of hairpin vortex

This section aims to provide insight into the formation processes of the MHVs and SHVs, and compare their generation mechanisms with those eddy packets in turbulence. POD is applied to extract the 3-D coherent structures. The generation, transport and reorientation of vorticity in the near wake are analysed.
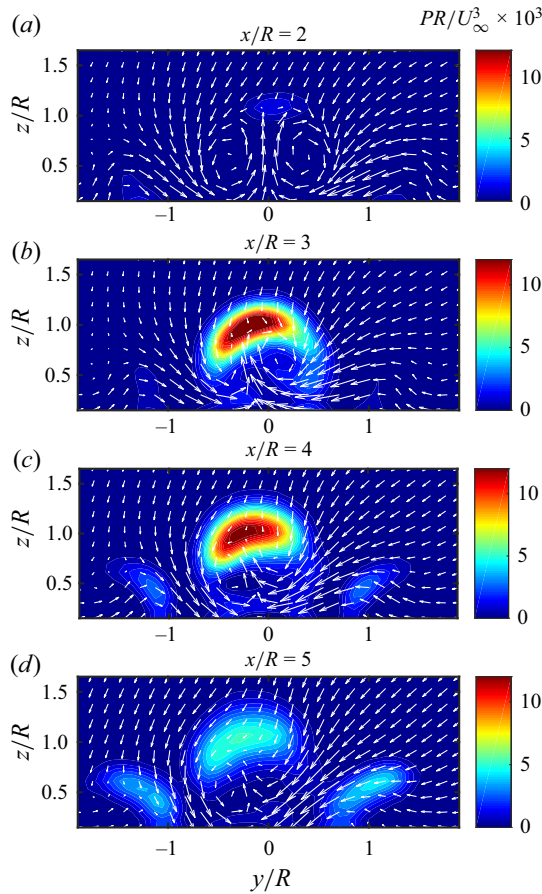
Figure 9. Distributions of the turbulence production in planes $x/R = 2, 3, 4, 5$. Projected quivers (white arrows) indicate in-plane time-averaged velocity vectors.

4.1. *Pattern of POD modes*

The POD analysis is performed on 1250 snapshots within the entire wake ($x/R \in [1, 8.6]$, $y/R \in [-2, 2]$, $z/R \in [0.1, 1.9]$) for all three velocity components. And the mean velocity is subtracted from the dataset before the POD calculation. The energy distribution ($\lambda_n / \sum \lambda_n$) for the first 45 POD modes, which contribute 50 % of the total energy, is shown in figure 10. A relatively 'flat' energy distribution is observed, indicating that the wake is highly unsteady three-dimensionally, and has multiple flow-scale structures. Nevertheless, the rapid decline in energy distribution for the first several modes is apparent, and the low energy percentage of the first several modes does not impact determination of the periodic/pseudo-periodic coherent feature as shown by the results below. The large-scale structures can be reconstructed sufficiently by applying the low-order model. In order to filter out small-scale structures, the investigation in the current subsection is based on the reconstructed flow that consists of POD modes containing 50 % of the total energy, and is projected on the mean velocity field, if there is no additional annotation. That is,

$$u_{reconstruct}(x, y, z, t) = \bar{u}(x, y, z) + \sum_{n=1}^{45} \alpha_n(t)\, \varphi_n(x, y, z). \tag{4.1}$$
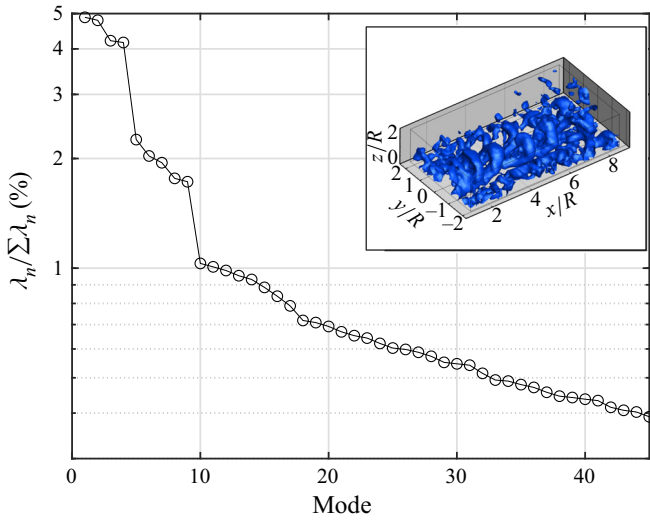
971 A36-16

Figure 10. Energy percentages of the first 45 POD modes, with inset showing the instantaneous field used for the decomposition.
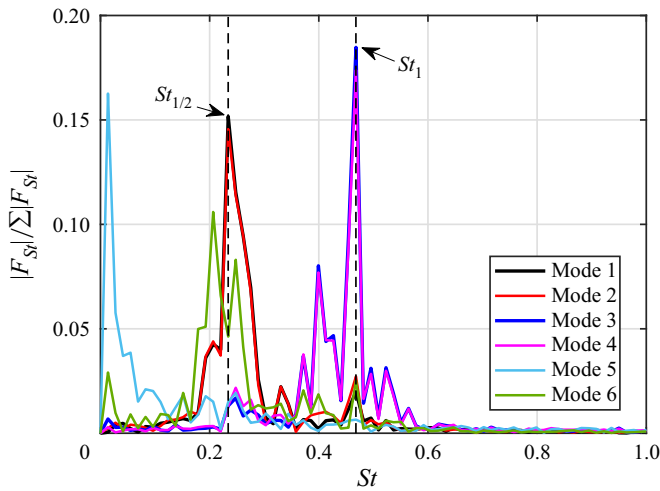

Figure 11. Spectrum diagram of time coefficients of the first six POD modes.

First, major features of periodicity of the near wake are investigated. By applying the Fourier transformation to the time coefficients, the spectral signatures of the first six main POD modes are investigated, with the energy of each mode being greater than 2 % of the total energy. As shown in figure 11, mode 1 (black curve) and mode 2 (red curve) are a pair of conjugated modes and share the same peak of Fourier coefficients $|F_{St}|$ at Strouhal number (St) 0.234, which is calculated by $St_{1/2} = f_{1/2}R/U_\infty$ ($f_{1/2} = 3.4$ Hz). Similarly, the spectrum profiles of mode 3 (blue curve) and mode 4 (magenta curve) are almost congruent, confirming that modes 3 and 4 compose another conjugated pair, with the peak at $St_1 = 0.468$ ($f_1 = 6.8$ Hz). Conversely, modes 5 and 6 are not congruent, and they exhibit lower dominant frequencies/Strouhal numbers. The pseudo-periodicity of the near wake reveals the existence of hairpin vortices, which originate from the Kelvin–Helmholtz (K–H) instability (Ye *et al.* 2016*a*).
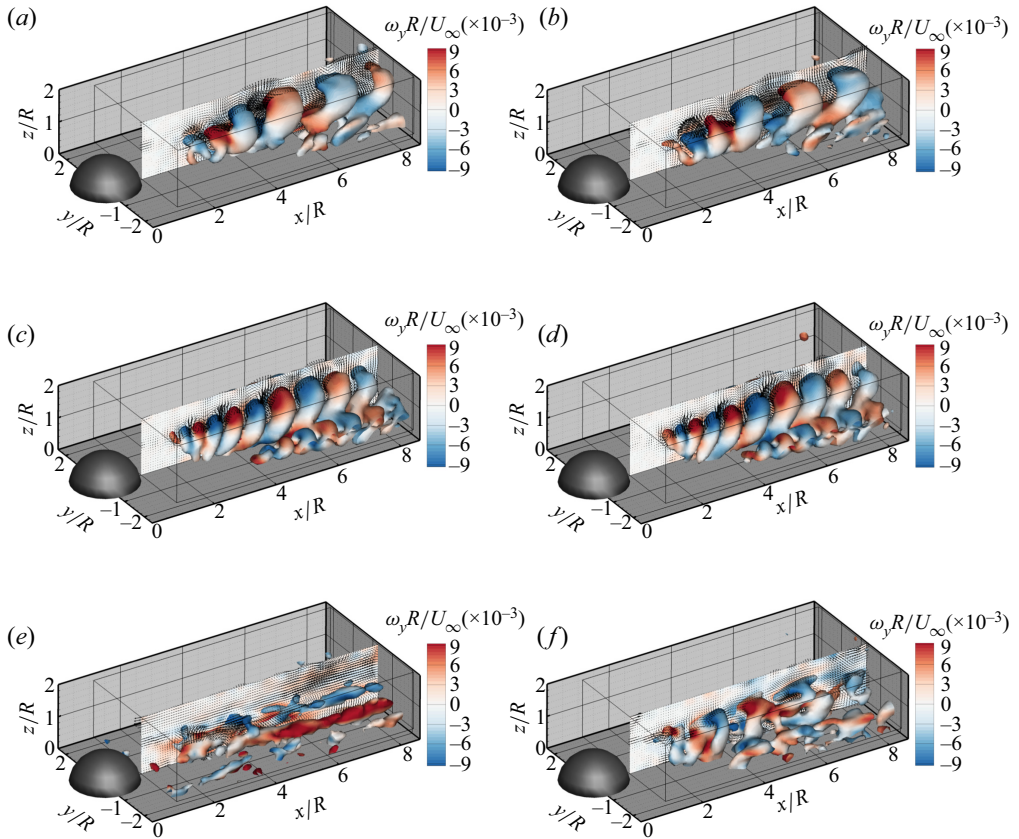
Figure 12. Isosurfaces of $\lambda_{ci} = 0.5\lambda_{ci,max}$ superimposed with the dimensionless streamwise vorticity contours and the dimensionless streamwise vorticity contours in the $y/h = 0$ plane of the first six POD modes at $Re_h = 1370$. (a–f) represent the structures of the first six modes, respectively.

Figure 12 further presents the spatial characteristics of the first six dominant POD modes at a typical moment, where the flow structures are visualized by the isosurfaces of $\lambda_{ci} = 0.5\lambda_{ci,max}$ superimposed with dimensionless spanwise vorticity contours. Mode 1 (figure 12a) and mode 2 (figure 12b) compose a pair of conjugated modes. Mode 3 (figure 12c) and mode 4 (figure 12d) constitute another conjugated pair. The vortical structures on both sides of the central plane reveal the SHV pattern and its periodic convective characteristic. In each conjugated pair, similar POD modes with shifting in the advection direction are presented, which is consistent with the fact that either the MHVs or the SHVs are travelling structures. It is worth noting that the MHVs appear in both pairs of conjugated POD modes, while the SHVs appear only in the second pair. Therefore, the MHVs and SHVs are both dominant structures, but the MHVs contribute a larger kinetic energy percentage than the SHVs do. Mode 5 (figure 12e) shows large-scale streamwise vortices with a low dominant frequency, which may be correlated with the legs of the hairpin vortices. The amount of small-scale structures has apparently increased in mode 6 (figure 12f). Indicated by their arch-like geometries, those structures still present a degree of correlation with the hairpin vortices. We infer that mode 6 reflects the deformation of the MHVs and SHVs. Briefly, in the hemisphere wake, the structures of hairpin vortices dominate the flow field and contribute a moderate percentage of the kinetic energy.
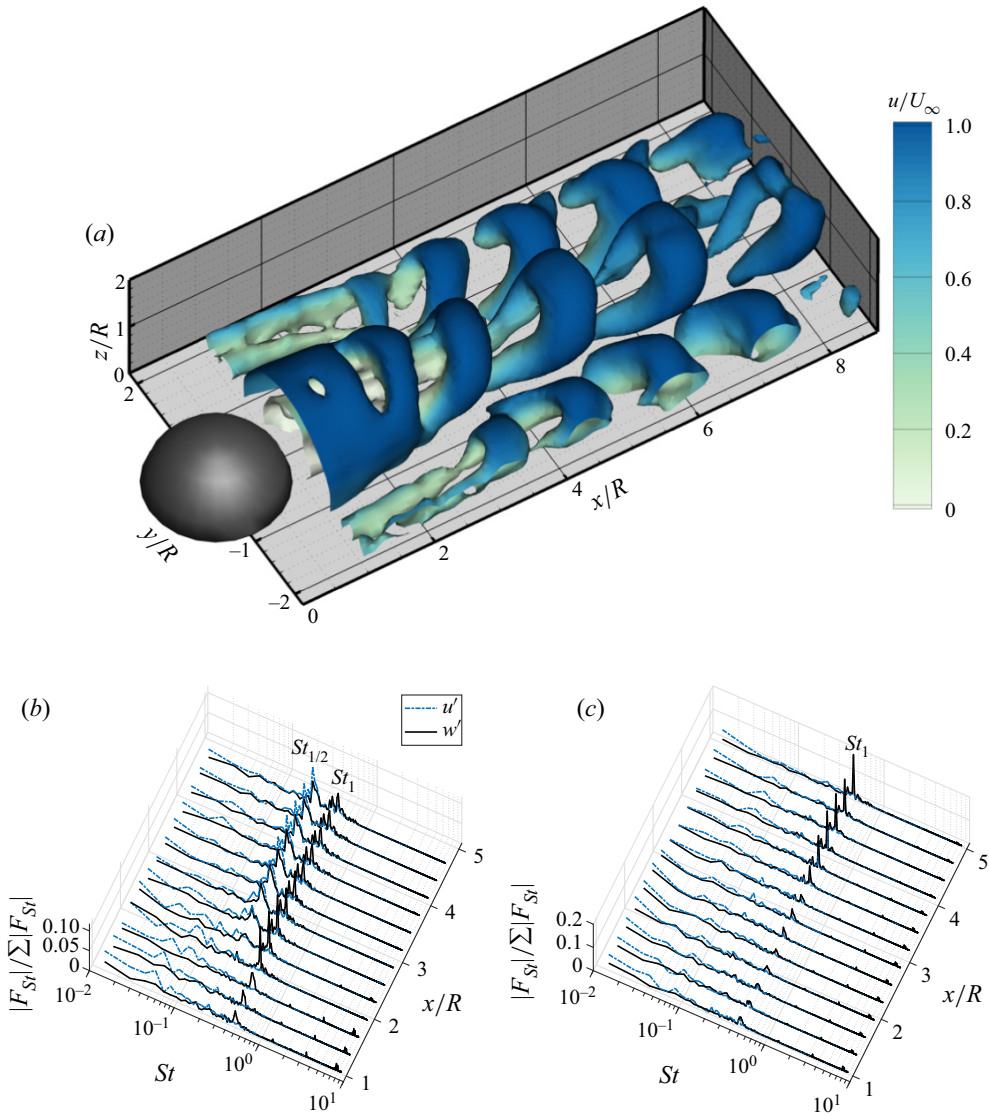
971 A36-18

Figure 13. (*a*) The hemisphere wake structures based on the first four POD modes with the mean flow. Isosurfaces of $\lambda_{ci} = 0.1\lambda_{ci,max}$ are superimposed with the dimensionless streamwise velocity contours. Frequencies of u and w components at the head portions of MHVs and SHVs with different streamwise locations are given in (*b,c*), respectively. For better display, the amplitude of the Fourier transformation is normalized by the sum of local amplitudes.

On the contrary, the streamwise vortices and other small-scale structures are less dominant in the wake, since the corresponding structures do not appear until mode 5 and mode 6, respectively.

Figure 13(*a*) shows a typical snapshot of the hemisphere wake based on the first four POD modes with the mean flow. Recall that in figure 4, a shear layer is formed downstream of the hemisphere. Around $x/R = 2.5$, the head portion of an MHV is generated and shed from the shear layer. Further downstream, the MHVs are fully formed, and their leg portions gradually approach the central plane $y/R = 0$. The MHVs incline

971 A36-19

towards the x direction since the upper parts of the MHVs have a higher streamwise convection velocity. This downstream inclination also implies that the mean shear flow, rather than Biot–Savart self-induction, dominates the dynamics of the near wake. The initial convection velocity estimated from the MHV head portion is $u_0 = 0.40 U_\infty$, and the MHVs are spaced at regular intervals of approximately $\lambda_0/R = 0.85$ in the near wake. The shedding frequency of the MHV is estimated to be $f_s = u_0/\lambda_0 = 6.8$ Hz, which is equal to the characteristic frequency f_1 of modes 3 and 4. The corresponding Strouhal number ($St = f_s R/U_\infty = 0.468$) is close to the upper end of the St range (0.2–0.5; Acarlar & Smith 1987a; Klebanoff, Cleveland & Tidstrom 1992) for the shedding phenomenon of roughness elements. According to the classical theory of K–H instability, the unstable wave moves with a phase velocity equal to the average velocity of the basic flow, namely, $u_{phase} \approx 0.4 U_\infty$ (see velocity profiles $x/R = 1.0$ and $x/R = 2.0$ in figure 6). Therefore, the characteristic frequency f_1 corresponds to the expected frequency due to K–H instability, which scales with u_{phase}/λ_0. The SHVs propagate at both sides of the MHVs. Combining figure 4, it is seen clearly that the SHVs are attached to the streamwise standing vortices in the near wake. Downstream of $x/R = 4$, the SHVs are detached from the standing vortices and fully formed. Streamwise and spanwise inclinations can also be observed during the downstream convection of the SHVs. The initial wavelength and convection velocity of the SHVs are estimated to $1.15R$ and $0.54 U_\infty$, respectively, resulting in a characteristic frequency 6.8 Hz.

Fourier transformation of velocity fluctuations u' and w' is executed at the region of head portions of the MHVs ($x/R \in [1.02, 5.17]$, $y/R = 0$, $z/R = 1.15$) and the SHVs ($x/R \in [1.02, 5.17]$, $y/R = -1.57$, $z/R = 0.69$) with different streamwise locations, to reveal significant information of pulsation caused by those spanwise-oriented vortical structures. As shown in figure 13(b), the dominant frequency of w' (black solid lines) is St_1 in the region of the shear layer. The corresponding amplitude increases during the MHV formation. On the contrary, the streamwise velocity fluctuations (blue dotted lines) present no apparent dominant frequency in the very near wake. After the shedding of the MHVs, the amplitude of St_1 decays gradually and the dominance switches from St_1 to $St_{1/2}$ for both u' and w'. Such a doubling relationship of the characteristic frequencies is also observed in figure 12, which reveals that the MHV region contains POD modes at frequencies St_1 and $St_{1/2}$. The dominance of the sub-harmonic would indicate an onset of vortex merging further downstream, which has been observed in K–H driven instability (Fang, Tachie & Dow 2022). The SHVs (figure 13c) contain only one dominant frequency, St_1, which can also be inferred from figures 11 and 12. Consistently, the formation frequency of the SHVs is the same as that of the MHVs. It is worth noting that the dominant frequency of w' even exists in the region of the standing vortex. In the current scenario, the source of velocity fluctuations would be the turbulence production or velocity pulsation raised by vortices. Considering that the turbulence production does not prevail in the very near wake (see figure 9), and no dominant vortical structures exist upstream of the SHV region except for the streamwise standing vortices (see figure 13a), the velocity fluctuations along the wall-normal direction are raised mainly by the streamwise standing vortices. The fluctuations in w periodically transport fluids between low- and high-speed regions, and eventually lead to the formation of the SHVs. Contrary to w', u' presents no apparent dominant frequency until the SHVs are formed. And u' is strengthened downstream in two aspects: the emergence of dominant frequency (see figure 13c) and the intensify of r.m.s. of u' (figure 7a). The former is related to the periodicity of SHV, and the latter is the result of transfer of mean flow kinetic energy into turbulence by the SHVs. Therefore, the
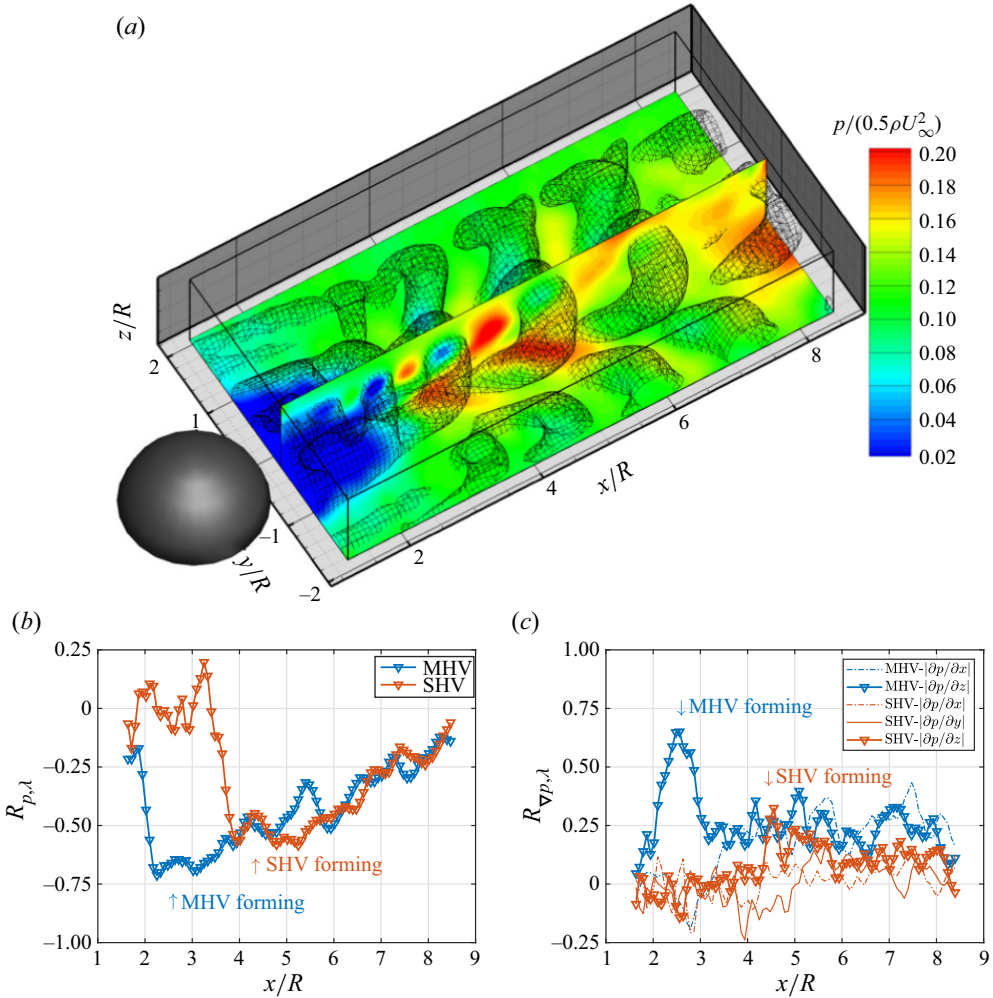
Figure 14. (*a*) Grid isosurfaces of λ_{ci} and the instantaneous dimensionless pressure contours in the $y/R = 0$ and $z/R = 0.16$ planes. (*b*) Correlation coefficients of λ_{ci} and pressure, and (*c*) correlation coefficients of λ_{ci} and pressure gradients, at the head portions of MHVs and SHVs with different streamwise locations.

fluctuations with a pulsatile mode in the u component is expected to be the result, not the cause, of the SHV formation.

As a supplement to figure 13, the corresponding instantaneous pressure is shown in figure 14(*a*), where the grid isosurfaces of λ_{ci} and the dimensionless pressure contours in the $y/R = 0$ and $z/R = 0.16$ planes are given. The low-pressure regions within the heads of the MHVs are apparent. The high-pressure regions between two adjacent vortex heads hint a deceleration of the flow at high wall-normal positions. To further understand the effect of pressure on the evolution of the hairpin vortices, the correlation coefficient $R_{p,\lambda}$ of time series of λ_{ci} and pressure at the regions of head portions of the MHVs and the SHVs (the same regions as studied in figure 13*b*,*c*) is investigated. Then $R_{p,\lambda}$ can be obtained from

$$R_{p,\lambda}(x_0, y_0, z_0, \Delta x, \Delta y, \Delta z) = \frac{\text{cov}(p(x_0, y_0, z_0), \lambda_{ci}(x_0 + \Delta x, y_0 + \Delta y, z_0 + \Delta z))}{\sigma_p \sigma_{\lambda_{ci}}},$$

(4.2)

where cov$(\cdot, \cdot)$ and σ represent covariance and standard deviation, respectively, (x_0, y_0, z_0) represents the point with the local maximum λ_{ci} value in the head portion at a certain streamwise location, and Δx, Δy and Δz are zeros when calculating the correlation between λ_{ci} and pressure at the same certain point. By calculating $R_{p,\lambda}$ at different streamwise locations, the correlation coefficient between λ_{ci} and pressure can be presented as a function of the streamwise location in figure 14(*b*). A large negative $R_{p,\lambda}$ could indicate the streamwise location where the pressure has a significant influence on the hairpin vortices, since λ_{ci} and the pressure are negatively correlated. Combined with figure 13, it can be seen that the strengthening of the negative correlation and the peak location generally agree with the shedding location and the intensification of velocity fluctuation at St_1, respectively. After shedding, the MHVs move downstream of the recirculation region, and the magnitude of $R_{p,\lambda}$ decreases. The downstream decreasing $R_{p,\lambda}$ indicates that the streamwise convection of the MHVs is less relevant to the pressure but more related to the kinematic reason, namely, the large streamwise velocity at a high wall-normal position. In regard to the SHVs, a similar pattern can be observed in the corresponding $R_{p,\lambda}$ curve. Namely, $R_{p,\lambda}$ reaches its peak approximately when the SHVs are fully developed, and then the magnitude of $R_{p,\lambda}$ decreases as the SHVs convect downstream.

Furthermore, the effects of different components of the pressure gradient on the vortical structures are discussed. The absolute values of the pressure gradients are used for the correlation to avoid the influence of the sign of pressure gradient on the calculation. Figure 14(*c*) reports the correlation coefficients between λ_{ci} and the streamwise (blue dash, labelled as 'MHV-$|\partial p/\partial x|$'), and the wall-normal (blue triangle, labelled as 'MHV-$|\partial p/\partial z|$') pressure gradients of the MHVs, the correlation coefficients between λ_{ci} and the streamwise (red dash, labelled as 'SHV-$|\partial p/\partial x|$'), spanwise (red solid line, labelled as 'SHV-$|\partial p/\partial y|$') and the wall-normal (red triangle, labelled as 'SHV-$|\partial p/\partial z|$') pressure gradients of the SHVs.

For the MHVs, the influence of the wall-normal pressure gradient is larger than that of the streamwise and spanwise pressure gradients. Specifically, the correlation coefficient of MHV-$|\partial p/\partial z|$ grows rapidly in the near wake, and then reaches its peak. During the formation of the MHVs, the head portion convects downstream and gradually leaves the low-pressure region. Thus the magnitude of the wall-normal pressure gradient $|\partial p/\partial z|$ increases with the downstream motion of the MHVs, and so does λ_{ci}. The increase of the MHV-$|\partial p/\partial z|$ correlation coefficient is synchronized with the magnification of velocity fluctuation with the characteristic frequency of St_1, and the peak location of MHV-$|\partial p/\partial z|$ also has a high agreement with the shedding location of the MHVs. The consistency of the evolution of λ_{ci}, velocity fluctuation and $|\partial p/\partial z|$ again confirms that the concentration of vorticity forming the MHVs is the reaction of the inward spiralling motion to the low-pressure region (Acarlar & Smith 1987*a*). As the MHVs convect further downstream, the influence of the wall-normal pressure gradient drops quickly. During this stage, the motion of an MHV is greatly maintained by the shearing from the high free-stream velocity. The correlation coefficient of SHV-$|\partial p/\partial z|$ exhibits a pattern similar to the $R_{p,\lambda}$ curve of the SHVs. Namely, the correlation coefficient of SHV-$|\partial p/\partial z|$ increases rapidly during the formation of the SHVs, and it decays downstream. Combined with figure 13, such a phenomenon again reveals the effect of velocity/pressure variation in the wall-normal direction on the formation of the hairpin vortices. The correlation coefficients of λ_{ci} and streamwise/spanwise pressure gradient, however, have relatively small magnitudes or even negative values before the formation of the hairpin vortices. Until the MHVs and SHVs are formed, the periodicity of streamwise/spanwise pressure gradient has a higher degree of correlation with that of the hairpin vortices. Therefore, it is

believed that the streamwise/spanwise pressure gradient plays a less significant role during the formation process.

4.2. *Generation of MHVs*

The above investigations clearly present the pseudo-periodicity of the near wake and reveal related dynamic causation. To further understand the formation mechanism of the MHVs, the transport of mass and vorticity in the near wake is investigated.

The left side of figure 15 shows the near wake λ_{ci} isosurfaces at $t = 0.4$ s, which are based on the first four POD modes with the mean flow for a clearer visualization. The MHV that is about to shed is labelled as 'A'. And the following downstream MHV, whose leg portion is formed, is labelled as 'B'. The top right plot of figure 15(a) gives the velocity distribution along the location line L1 ($x/R = 1.79$, $y/R = -0.81$, $z/R \in [0.15, 1.00]$), which crosses through the forming leg portion of A. The normalized streamwise component u^* (black line) increases with a higher wall-normal position, which leads to the streamwise incline of MHV. The spanwise component v^* (blue line) deviates from zero and becomes positive near the wall. Although v^* maintains a relatively small value, it induces the leg portion to incline towards the central plane $y/R = 0$. The wall-normal component w^* (red line) is negative along L1, implying the mass transport from the head portion to the leg portion. Considering that rotating in the x–y plane should represent the main characteristics of vortical structures along L1, the non-dimensional vorticity transport equation in the z direction, which reads

$$\frac{\partial \omega_z^*}{\partial t^*} + (\boldsymbol{u}^* \cdot \boldsymbol{\nabla}^*)\omega_z^* = (\boldsymbol{\omega}^* \cdot \boldsymbol{\nabla}^*)w^* + \frac{1}{Re}\nabla^{*2}\omega_z^*, \tag{4.3}$$

is thus the focus of the following discussion. The tilting term can be further expanded as

$$(\boldsymbol{\omega}^* \cdot \boldsymbol{\nabla}^*)w^* = \underbrace{\omega_x^* \frac{\partial w^*}{\partial x^*}}_{T_{x\Rightarrow z}^*} + \underbrace{\omega_y^* \frac{\partial w^*}{\partial y^*}}_{T_{y\Rightarrow z}^*} + \underbrace{\omega_z^* \frac{\partial w^*}{\partial z^*}}_{S_z^*}, \tag{4.4}$$

and the concerned vorticity convection term in the z direction ($w^*(\partial\omega_z^*/\partial z^*)$) is denoted as C_z^*. Wall-normal vorticity ω_z^* and its convection (C_z^*), tilting ($T_{x\Rightarrow z}^*$, $T_{y\Rightarrow z}^*$) and stretching (S_z^*) terms along L1 are shown in the bottom right plot of figure 15(a). From $z/R = 1$ to the near-wall position, ω_z^* (black solid line) reaches its maximum at $z/R = 0.7$ then gradually decreases. As indicated by the convection term (green dotted line), the downward convection of positive ω_z^* (positive convection $C_z^{(+)}$ towards negative convection $C_z^{(-)}$) feeds wall normal vorticity from the high position to the low position. The tilting term $T_{x\Rightarrow z}^*$ (red dotted line) is approximately equal to zero, indicating no significant tilting from streamwise vorticity into the wall-normal direction. On the contrary, the $T_{y\Rightarrow z}^*$ tilting effect (blue dotted line) is relatively strong when $z/R > 0.5$. Note that ω_z^* and $T_{y\Rightarrow z}^*$ have the same sign here. Therefore, the tilting term $T_{y\Rightarrow z}^*$ makes a positive contribution to the change of ω_z^*. And the forming leg portion inclines towards the spanwise side via vortex tilting. The stretching term S_z^* is greater than zero when $z/R > 0.65$, which confirms the stretching of the vortex tube and the increase of vorticity during the formation process of the leg portion. As the absolute values of w^* and ω_z^* decrease simultaneously near the wall, a compressing effect is expected, which is revealed by the fact $S_z^* < 0$ when $z/R < 0.65$. Briefly, mass and vorticity transport is from the upper part to the lower part during the formation of the MHVs.
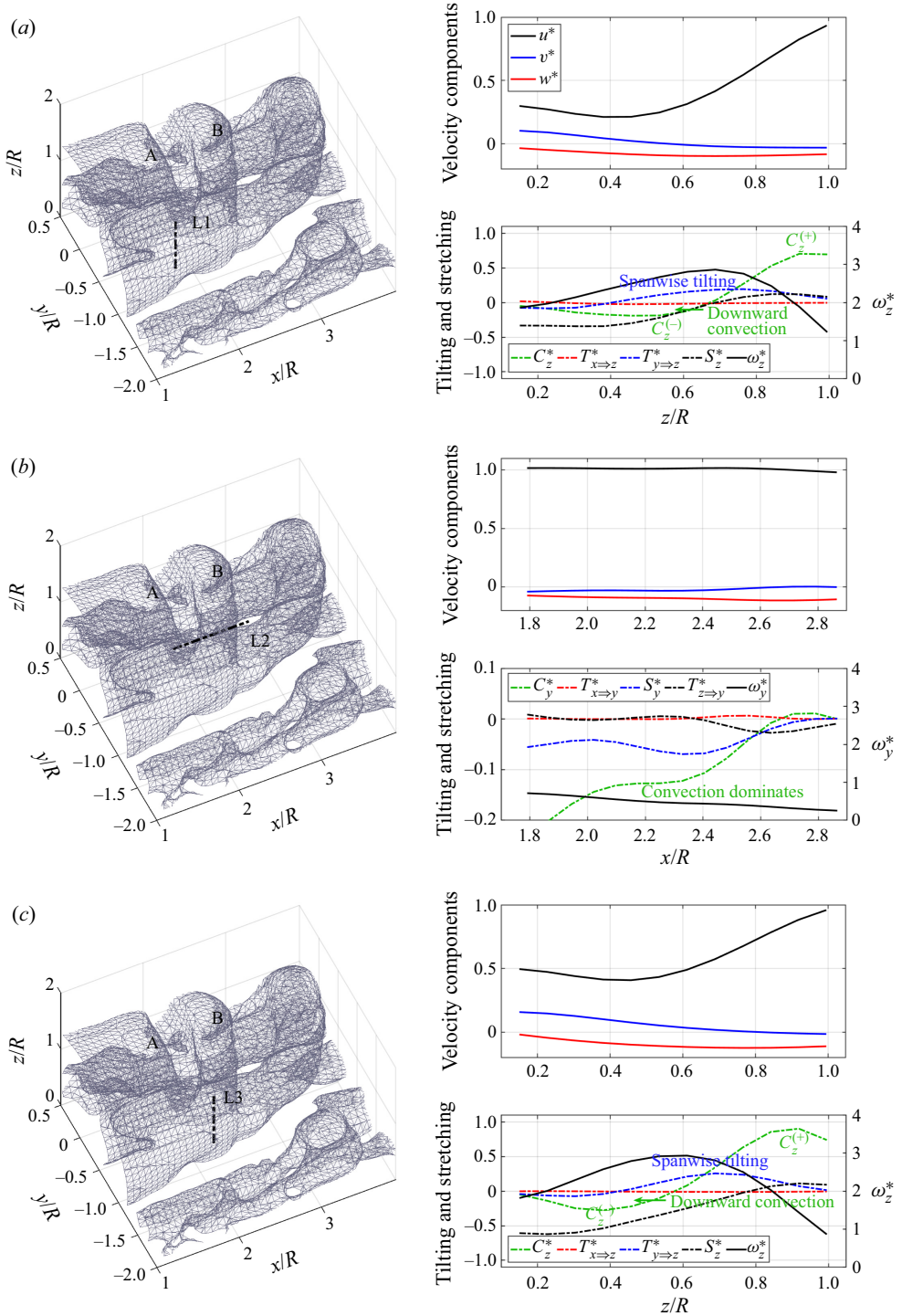
Figure 15. Mass and vorticity transport along characteristic lines in the MHV region. Dimensionless terms are marked with an asterisk.

Another location line L2 ($x/R \in [1.79, 2.87]$, $y/R = -0.72$, $z/R = 1.15$), which crosses through the MHVs A and B, is chosen to understand the deformation, mass and vorticity transport after the shedding of the head portion. The velocity distribution along L2 is shown in the top right plot of figure 15(b). The u^* component is close to the free-stream speed, while the v^* component stays around zero. Hence the upper part of an MHV does not incline towards the central plane, which is different from the behaviour of its lower part (i.e. the leg portion). The negative w^* component again implies the mass transport from the head portion to the leg portion. Since L2 is closer to the head portion, the vorticity equation in the y direction is investigated. The corresponding tilting term can be expanded as

$$(\boldsymbol{\omega^*} \cdot \boldsymbol{\nabla^*})v^* = \underbrace{\omega_x^* \frac{\partial v^*}{\partial x^*}}_{T_{x \Rightarrow y}^*} + \underbrace{\omega_y^* \frac{\partial v^*}{\partial y^*}}_{S_y^*} + \underbrace{\omega_z^* \frac{\partial v^*}{\partial z^*}}_{T_{z \Rightarrow y}^*}, \tag{4.5}$$

and the concerned vorticity convection term in the y direction ($v^*(\partial \omega_y^*/\partial y^*)$) is denoted as C_y^*. As shown in the bottom right plot of figure 15(b), the spanwise vorticity ω_y^* decreases slightly along L2. Recall that the v^* component is negative, hence the negative C_y^* may imply the convection of spanwise vorticity from the central plane. Here, S_y^* is negative and its magnitude decreases gradually along L2, which denies the stretching of MHV in the y direction. It is worth mentioning that the tilting terms $T_{x \Rightarrow y}^*$ (red dotted line) and $T_{z \Rightarrow y}^*$ (black dotted line) are approximately equal to zero, indicating that no strong tilting effects exist at the upper part of an MHV. Instead, the vorticity convection dominates, which contributes to the vorticity redistribution during the formation of the upper part of an MHV.

To further illustrate the mass and vorticity transport inside the MHV B that is already shed, relevant terms along L3 ($x/R = 2.25$, $y/R = -0.81$, $z/R \in [0.15, 1.00]$) are investigated (figure 15c). Similar to the observation of L1, the vorticity equation in the z direction is the focus of discussion. In general, the distributions of velocity components and vorticity convection/tilting terms have patterns similar to the terms along L1. Hence the downward mass and vorticity transport is still expected after the formation of the leg portion. The tilting term $T_{x \Rightarrow z}^*$ (red dotted line) is still close to zero when the MHV B has just been shed. The magnitude of $T_{x \Rightarrow z}^*$ is expected to increase downstream, where the MHVs incline towards the streamwise direction. Compared with figure 15(a), the tilting term $T_{y \Rightarrow z}^*$ (blue dotted line) has a higher magnitude along L3. Therefore, a stronger tilting effect of spanwise vorticity into the wall-normal direction is implied, which is consistent with the continuous approach of the MHV legs to each other when convecting downstream (see figure 13). In addition, no wall-normal stretching effect acts on the formed leg portion of the MHV B.

Based on the analysis above, the formation process of an MHV is observed clearly and sketched in figure 16. A shear layer is formed downstream of the hemisphere and entrains fluid continuously into the interior of the shear layer. During the downstream convection of the shear layer, an arch-like vortex tube with strong vorticity is generated. Subsequently, the vortex tube grows gradually and is shed from the shear layer. And the upper portion of the vortex tube evolves into the head of an MHV. The formation and shedding of the MHV head are caused by the K–H instability in the curved shear layer and concentration of vortex lines (Carr & Plesniak 2016; Johnson *et al.* 2017). During these processes, mass and vorticity transport from the upper to the lower portions contributes to the formation of the legs of the MHV. Therefore, during the generation of an MHV, the head of the vortex
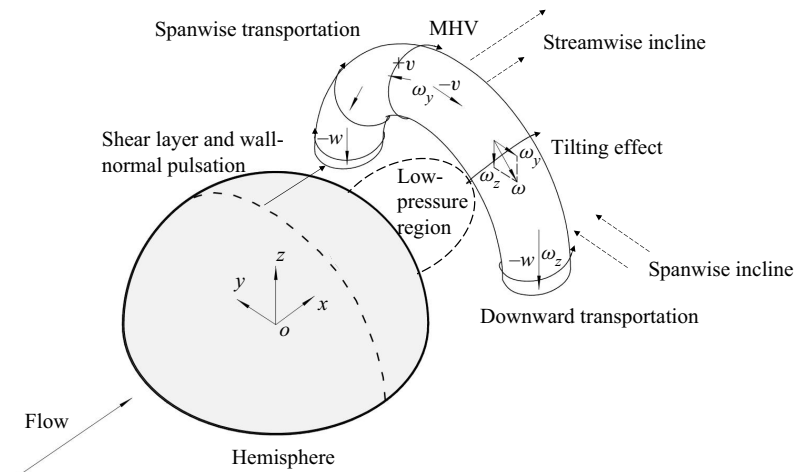
Figure 16. Sketch of the formation and development mechanism of the MHV.

is always formed first, followed by the formation of the legs of the vortex. In addition, the inward velocity and tilting effect also contribute to the deformation of the MHV when convecting downstream, i.e. the spanwise incline and migration of the legs to each other.

The aforementioned MHV formation process reveals significant similarities and differences between hairpin vortices in the laminar regime and the turbulent regime. Though a universal agreement on the generation mechanism of hairpin vortices in turbulence has not been reached ultimately, previous studies (Robinson 1991; Adrian 2007) have pointed out that the vertical perturbation brings low-speed fluids to higher wall-normal positions and therefore leads to the creation of vorticity and rolling-up of hairpin vortices. Thus the role of wall-normal velocity fluctuation from the presence of the hemisphere in the formation of the MHVs would be akin to the role of vertical perturbation in the hairpin vortex formation in turbulent boundary layers. Intuitively, the similarities in geometry and formation mechanism between the MHVs and hairpin vortices in TBLs would shed light on the further investigation of the latter. However, we must also notice that the causation of the MHV formation is the obstructive effect of the hemisphere on flow, instead of vertical perturbations on spanwise vortices or ejection motions induced by quasi-streamwise vortices. Hence the head and leg portions of an MHV are formed in an order due to stronger shearing effect and convection speed at higher wall-normal positions, whereas some conceptual models (Theodorsen 1952; Hinze 1975) suggest that the head and legs of a newly generated hairpin vortex in the turbulent regime usually appear simultaneously, if it is evolved from a spanwise vortex. The discrepancy in formation processes between the MHVs and hairpin vortices in TBLs is a manifestation of their different causes of formation.

4.3. *Generation of SHVs*

Several studies (Acarlar & Smith 1987a; Ye *et al.* 2016b) have investigated the topology and propagation of SHVs. On the basis of predecessors, the current study investigates explicitly the evolution of an SHV and suggests a detailed formation mechanism of this coherent structure. As illustrated in figure 4, the counter-rotating vortex pair consisting of the primary standing vortex PSV1 and the secondary standing vortex SSV1 bypasses the hemisphere into the wake along the streamwise direction. At $x/R = 3.2$, an SHV
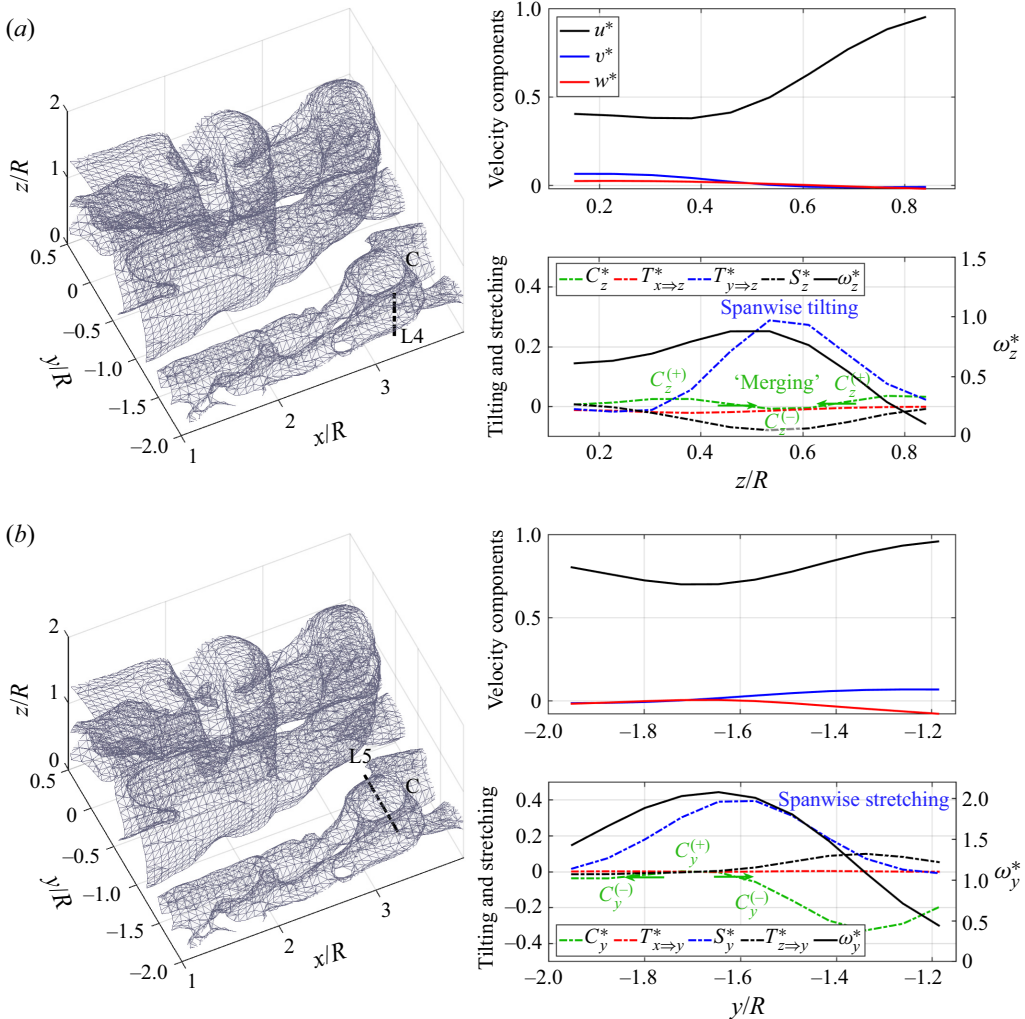
Figure 17. Mass and vorticity transport along representative lines in the SHV region. Dimensionless terms are marked with an asterisk.

(labelled as 'C') is observed to be formed from PSV1 and SSV1, as shown in the left of figure 17. A vertical location line L4 ($x/R = 3.25$, $y/R = -1.88$, $z/R \in [0.15, 0.84]$) is chosen to investigate transport terms inside the forming leg portion of C. As shown in the top right plot of figure 17(a), the u^* component increases with an increasing wall normal position, leading to the streamwise incline of the SHV. The v^* component decreases gradually and becomes negative when $z/R > 0.5$. Similarly, the w^* component decreases gradually, but it does not become negative until $z/R = 0.7$. Therefore, the mass transport in the leg portion of the SHV includes upward transport from the lower part and downward transport from the head portion. Since the swirling in the x–y plane dominates along L4, the vorticity equation in the z direction is studied. As seen in the bottom right plot of figure 17(a), the dimensionless ω_z^* (black solid line) is positive along L4, and its distribution is similar to that of ω_z^* along L3 (figure 15c). Combined with the distribution of the w^* component, the convection term (green dotted line) indicates vorticity convection

from the lower and upper parts to the middle ($C_z^{(+)}$ regions exist at both ends of L4, and the $C_z^{(-)}$ region is at $z/R = 0.6$). This mode of transport indicates a 'bridging' phenomenon, implying that the SHV formation is predominated by the induction of the streamwise standing vortex pair. Sabatino & Rossmann (2015) also observed a similar 'bridging' phenomenon during the formation of a secondary hairpin vortex, which is initiated by the ejected fluids between the elongated legs of the primary hairpin vortex. The tilting term $T_{x\Rightarrow z}^*$ (red dotted line) with a small magnitude implies the minor tilting effect between the x and z directions. The strong $T_{y\Rightarrow z}^*$ effect (blue dotted line) benefits the accumulation of ω_z^* and contributes to the spanwise incline of the SHVs, as seen in figure 13. There is no stretching effect along L4 since the term S_z^* (black dotted line) is negative. This differs from the conceptual model proposed by Theodorsen (1952), which states that the leg portion would be stretched during the formation of a hairpin vortex.

Distributions of velocity components along the location line L5 ($x/R = 3.25$, $y/R \in [-1.95, -1.18]$, $z/R = 0.69$) are studied to understand mass transport inside the head portion of the SHV, as shown in figure 17(*b*). The u^* component presents a large magnitude, since the head portion is at a high wall-normal position. The v^* component is negative when $y/R < -1.7$, and changes its sign at the mid-span of the head portion. The w^* component is negative at both ends of L5. Combined with the distributions of v^* and w^* components, the downward mass transport from the head portion is revealed, which is consistent with the 'bridging' phenomenon found along L4. The dimensionless ω_y^* (black solid line) is positive and reaches its maximum at the mid-span of the head. The convection term (green dotted line) along with the v^* component indicates the transport of positive spanwise vorticity from the mid-span of the head to both legs ($C_y^{(-)}$ regions exist at both ends of L5, and the $C_y^{(+)}$ region is at $y/R = -1.7$). Here, $T_{x\Rightarrow y}^*$ (red dotted line) and $T_{z\Rightarrow y}^*$ (black dotted line) are small, thus implying limited tilting effects. On the contrary, the term S_y^* (blue dotted line) has a high magnitude, which reveals clearly the strong spanwise stretching effect related to the formation of the head portion (i.e. local increase of ω_y^*). It is believed that the main reason for the kinematic inducement of the vorticity generation is the induction of the streamwise standing vortex pair rather than the induction of the MHVs. Otherwise, the SHVs would incline to the MHVs due to the lateral motions of the fluid generated by the MHVs, similar to the behaviour of subsidiary vortices observed by Haidari & Smith (1994).

Based on the investigations above, the SHV formation process is analysed and sketched in figure 18. The standing vortices bypass the hemisphere then have the same rotating pattern as in the legs of the MHV. The flow in the interior of the standing vortex pair is induced to lift up and interact with the high-speed flow at a higher wall-normal position, which creates a local velocity gradient and further results in the generation of vorticity. With the entrainment of nearby fluid and the increase of vorticity, a new arch-like vortex tube is produced and grows gradually as the SHV head portion. Mass and vorticity transport from the head portion and the streamwise standing vortices to each other leads to the formation of the SHV legs. Hence the SHV can be regarded as the bridging of the standing vortices during the downstream convection. With the detachment of the legs from the standing vortex pair, a fully developed SHV is formed.

Although the velocity fluctuation in the wall-normal direction plays an important role in the formation of the hairpin vortices, the generation inducements of the MHVs and SHVs are different. The former originates from K–H instability in the shear layer, while the latter is the production of the lifting-up flows induced by the streamwise standing vortices.
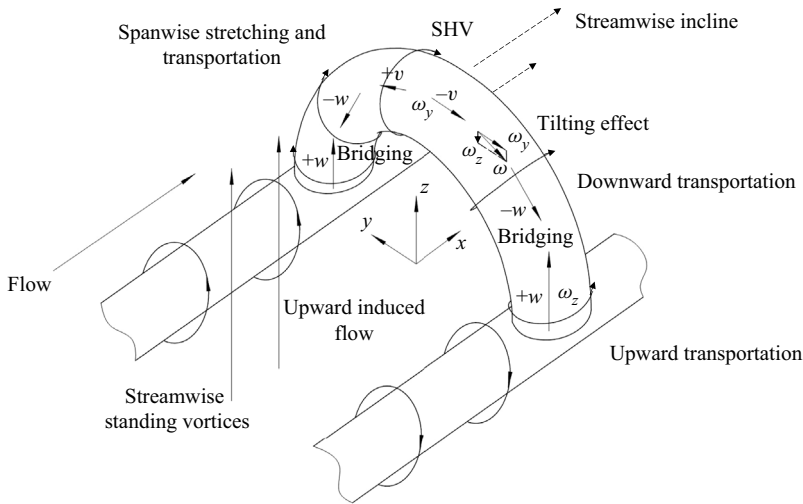
Figure 18. Sketch of the formation and development mechanism of the SHV.

Such a difference leads to the variation in their formation processes. Contrary to the generation of the MHVs, the leg portion forms earlier than the head portion does during the generation of the SHVs. The system of SHVs presents a degree of similarity to the conceptual model of wall turbulence proposed by Robinson (1991): the flow from the near-wall region is lifted upwards by the quasi-streamwise vortices; the existence of the SHVs results in the occurrence of sweeping/ejecting motions (Q2/Q4 events) distributed in the head portion. It is worth noting that the streamwise vortices are generated due to the obstacle of the hemisphere in the current scenario, which differs from the self-sustaining process or mechanisms explaining the origination of quasi-streamwise vortices in TBLs. Nevertheless, the formation process of the SHVs is similar to the regeneration process of hairpin vortices reported by previous studies (Zhou *et al.* 1999; Sabatino & Rossmann 2015) and the generation of hairpin vortices in TBLs due to the connection of streamwise vortices found by Wang, Huang & Xu (2015) and Jodai & Elsinga (2016). Thus the observation of an SHV would contribute to the study of hairpin vortices in TBLs.

5. Conclusions

The present study investigates qualitatively and quantitatively the time-averaged and instantaneous three-dimensional (3-D) velocity and reconstructed pressure fields in the near-wake field behind a hemisphere at Reynolds number $Re_r = 1370$. Time-resolved TPIV measurement is utilized to conduct this investigation. Multiple analysis approaches, such as Fourier transformation, POD and pressure reconstruction, are adopted. The results provide insights into the hairpin vortex structures in the laminar boundary layer and details of corresponding formation mechanisms, which would facilitate the study on evolution of hairpin vortices in the turbulent regime.

The main hairpin vortices (MHVs) and side hairpin vortices (SHVs) are formed periodically in the rear and both sides of the hemisphere, the periodicity of which is revealed clearly by the dominant POD modes and fluctuations in velocity components. The velocity fluctuation and pressure gradient in the wall-normal direction are shown to be highly correlated with the formation of the MHVs and SHVs, indicating the importance of wall-normal variations for the formation of the hairpin vortices. With the continuous

entrainment of fluid and feeding of vorticity, the head portion of an MHV is formed first and shed from the shear layer. The generation of the head portion is followed by the leg portion formation due to the transport of mass and vorticity from the upper to the lower parts. The differences of convection speeds, tilting and stretching effects further promote the formation of the leg portion and the completion of the MHV structure.

In contrast to the MHVs, the SHVs are formed first with their leg portions. Benefiting from the time-resolved TPIV, details of SHVs are revealed significantly, and show that this vortex structure actually originates from the standing vortices. The standing vortex pairs that coincide with the rotating direction of the legs of MHV extend downstream and eject the fluid near the wall to higher positions. As a result, the leg portion is formed first, then the interaction between the upward induced flow and the high-speed incoming flow leads further to the formation of the head portion. The transport of mass and vorticity from the head and leg portions to each other finally connects these two portions, and an SHV is thereby generated completely. As far as the authors are aware, these are the first time-resolved 3-D results that investigate experimentally the formation of the SHVs. The formation process is akin to the generation process of hairpin vortices in laminar and turbulent boundary layers. Compared with the MHVs, the SHVs exhibit more similarities to hairpin vortices in TBLs, making them more suitable to be investigated as the reference for the study of evolutionary dynamics in the latter.

Declaration of interests. The authors report no conflict of interest.

Author ORCIDs.

- Han Tu https://orcid.org/0000-0001-7355-2912;
- Qi Gao https://orcid.org/0000-0002-2532-0997;
- Wenxuan She https://orcid.org/0000-0002-7609-669X;
- Jinjun Wang https://orcid.org/0000-0001-9523-7403.

Appendix A. Undisturbed boundary layer profile

The validation of the laminar boundary layer developing along the flat plate without the hemisphere at $Re_r = 1370$ was conducted using planar PIV. As shown in figure 19(*a*), the planar PIV system consisted of a 5 W continuous laser source and a charge-coupled device (CCD) camera. The laser sheet was approximately 1 mm thick and was oriented to be parallel to the x–z plane and cross the mid-span of the flat plate. The focal length of the camera lens was 45 mm, and the resolution of the CCD camera was 640×480 pixels. The measurement size was $28 \text{ mm} \times 21 \text{ mm}$, and the magnification was $0.044 \text{ mm pixel}^{-1}$. Hollow glass particles with mean diameter 10 μm and density 1.05 g cm^{-3} were used as tracers. The initial interrogation window was 64×64 pixels, and the final interrogation window size was 16×16 pixels, with three refinement steps. The overlap rate was 50 %, and the deformation iteration (Scarano 2002) was performed twice during each step. After a sub-pixel fitting, the uncertainty of the pixel displacement could reach down to 0.1 pixels. The planar PIV calibration, data acquisition and data processing were conducted on the PIV software MicroVec 3.6.2 (MicroVec., Inc.).

The velocity profile at $x/R = -1$ (the streamwise location of the hemisphere leading edge) from the planar PIV measurement is compared with the theoretical solution based on Blasius self-similarity, as shown in figure 19(*b*). The agreement confirms the laminar regime of the undisturbed boundary layer.
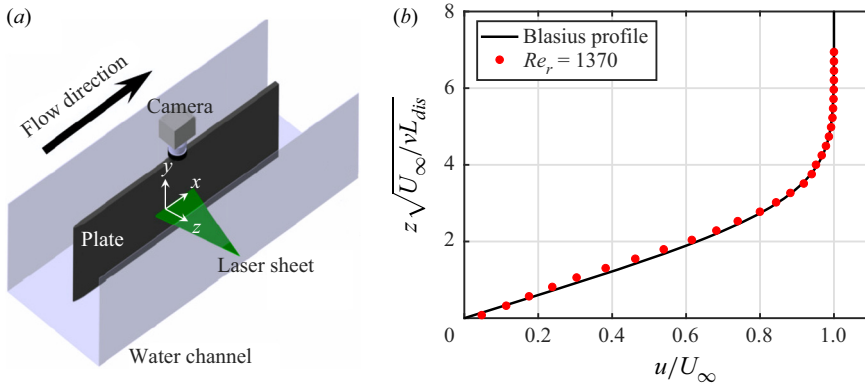
Figure 19. (*a*) Sketch of the planar PIV for the validation of the laminar boundary layer; the coordinate system is the same as that of the TPIV measurements. (*b*) Comparison of the undisturbed boundary layer profile at $x/R = -1$ and the Blasius solution.
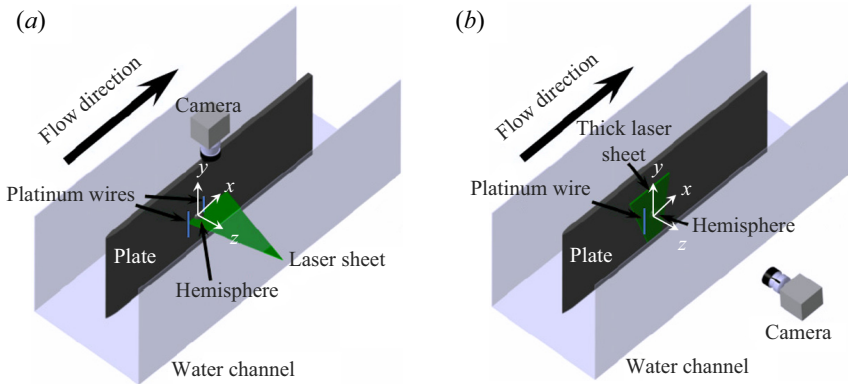

Figure 20. Sketches of the hydrogen-bubble visualization from (*a*) the side view and (*b*) the top view. Note that the origin of the coordinate system is at the centre of the hemisphere bottom surface.

Appendix B. Hydrogen-bubble visualization

The distribution of the standing vortices and corresponding streamwise inheritors is of particularly interest. Hydrogen-bubble visualization from the side and top views was conducted, serving as a supplement to the TPIV measurements. The arrangement of the hydrogen-bubble visualization is shown in figure 20.

Visualizations of individual standing vortices are superimposed together in figure 21(*a*) for better presentation of the standing vortex system. The primary standing vortex 1 (PSV1) is formed due to the obstacle of the hemisphere on the flow convection. PSV1 and the induced secondary standing vortex 1 (SSV1) consist further of a pair of counter-rotating vortices. Subject to the induction of PSV1 and SSV1, a fluid material surface is formed in front of the hemisphere, which can be considered as an extended upstream protuberance. As a result, a new standing vortex PSV2 and derivative vortical structures are formed, which is similar to the formation of PSV1 and SSV1. Further downstream, the re-orientation of the standing vortices to the streamwise direction is observed clearly from the top view (figure 21*b*).
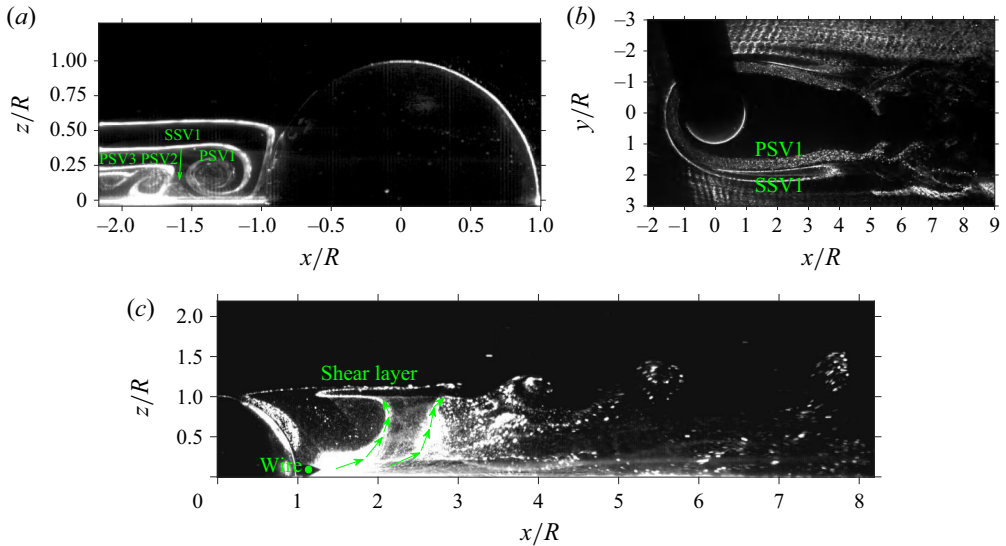
Figure 21. (*a*) Overlapped side view of standing vortices. (*b*) Top view of standing vortices. (*c*) Side view of hairpin vortex structures.

The general distribution of the hairpin vortices is revealed directly by the side view visualization shown in figure 21(*c*), which also helps to locate the shedding position. The shear layer is detached from the top of the hemisphere. As one can expect, hairpin vortices originated from the K–H instability are formed and shed periodically from the curved shear layer. Indicated by the geometries of clusters of bubbles (highlighted by green arrows, i.e. a visualization of near-wake streaklines), the recirculating effect in the rear of the hemisphere and the shedding of hairpin vortices around $x/R = 2.5$ are clearly seen. Further downstream, the sequentially shed hairpin vortices are observed.

REFERENCES

ACARLAR, M.S. & SMITH, C.R. 1987*a* A study of hairpin vortices in a laminar boundary layer, Part 1: hairpin vortices generated by a hemisphere protuberance. *J. Fluid Mech.* **175**, 1–41.

ACARLAR, M.S. & SMITH, C.R. 1987*b* A study of hairpin vortices in a laminar boundary layer, Part 2: hairpin vortices generated by fluid injection. *J. Fluid Mech.* **175**, 43–83.

ADHIKARI, D. & LONGMIRE, E.K. 2013 Infrared tomographic PIV and 3D motion tracking system applied to aquatic predator–prey interaction. *Meas. Sci. Technol.* **24**, 024011.

ADRIAN, R.J. 2007 Hairpin vortex organization in wall turbulence. *Phys. Fluids* **19**, 041301.

ADRIAN, R.J., MEINHART, C.D. & TOMKINS, C.D. 2000 Vortex organization in the outer region of the turbulent boundary layer. *J. Fluid Mech.* **422**, 1–54.

BAUR, T. 1999 PIV with high temporal resolution for the determination of local pressure reductions from coherent turbulence phenomena. In *Proceedings of the 3rd International Workshop on PIV – Santa Barbara*, pp. 101–106.

BELKHOU, H., RUSSEIL, S., DBOUK, T., MOBTIL, M., BOUGEARD, D. & FRANCOIS, N.Y. 2019 Large eddy simulation of boundary layer transition over an isolated ramp-type micro roughness element. *Intl J. Heat Fluid Flow* **80**, 108492.

CAI, S., WANG, Z., FUEST, F., JEON, Y., GRAY, C. & KARNIADAKIS, G. 2021 Flow over an espresso cup: inferring 3-D velocity and pressure fields from tomographic background oriented Schlieren via physics-informed neural networks. *J. Fluid Mech.* **915**, A102.

CAO, Y. & TAMURA, T. 2020 Large-eddy simulation study of Reynolds number effects on the flow around a wall-mounted hemisphere in a boundary layer. *Phys. Fluids* **32** (2), 025109.

CARR, I.A., BERATLIS, N., BALARAS, E. & PLESNIAK, M.W. 2020 Effects of highly pulsatile inflow frequency on surface-mounted bluff body wakes. *J. Fluid Mech.* **904**, A29.

CARR, I.A. & PLESNIAK, M.W. 2016 Three-dimensional flow separation over a surface-mounted hemisphere in pulsatile flow. *Exp. Fluids* **57** (1), 9.

CHERUBINI, S., DE TULLIO, M., DE PALMA, P. & PASCAZIO, G. 2013 Transient growth in the flow past a three-dimensional smooth roughness element. *J. Fluid Mech.* **724**, 642–670.

CHRISTENSEN, K. & ADRIAN, R. 2002 Measurement of instantaneous Eulerian acceleration fields by particle image accelerometry: method and accuracy. *Exp. Fluids* **33** (6), 759–769.

CITRO, V., GIANNETTI, F., LUCHINI, P. & AUTERI, F. 2015 Global stability and sensitivity analysis of boundary-layer flows past a hemispherical roughness element. *Phys. Fluids* **27** (8), 084110.

CORINO, E. & BRODKEY, R. 1969 A visual investigation of the wall region in turbulent flow. *J. Fluid Mech.* **37** (1), 1–30.

DABIRI, J.O., BOSE, S., GEMMELL, B.J., COLIN, S.P. & COSTELLO, J.H. 2014 An algorithm to estimate unsteady and quasi-steady pressure fields from velocity field measurements. *J. Expl Biol.* **217** (3), 331–336.

DENG, S., PAN, C. & WANG, J. 2014 Dynamics of low-speed streak evolution and interaction in laminar boundary layer. *Acta Mechanica Sin.* **30** (5), 636–645.

DISCETTI, S., NATALE, A. & ASTARITA, T. 2013 Spatial filtering improved tomographic PIV. *Exp. Fluids* **54** (4), 1–13.

EITEL-AMOR, G., ÖRLÜ, R., SCHLATTER, P. & FLORES, O. 2015 Hairpin vortices in turbulent boundary layers. *Phys. Fluids* **27**, 025108.

ELSINGA, G.E., SCARANO, F., WIENEKE, B. & VAN OUDHEUSDEN, B.W. 2006 Tomographic particle image velocimetry. *Exp. Fluids* **41**, 933–947.

ESHBAL, L., RINSKY, V., DAVID, T., GREENBLATT, D. & VAN HOUT, R. 2019 Measurement of vortex shedding in the wake of a sphere at $Re = 465$. *J. Fluid Mech.* **870**, 290–315.

FANG, X., TACHIE, M. & DOW, K. 2022 Turbulent separations beneath semi-submerged bluff bodies with smooth and rough undersurfaces. *J. Fluid Mech.* **947**, A19.

GAO, Q., ORTIZ-DUEÑAS, C. & LONGMIRE, E.K. 2011 Analysis of vortex populations in turbulent wall-bounded flows. *J. Fluid Mech.* **678**, 87–123.

GAO, Q., WANG, H. & SHEN, G. 2013 Review on development of volumetric particle image velocimetry. *Chinese Sci. Bull.* **58** (36), 4541–4556.

GAO, T., SUN, J., CHEN, W., FAN, Y. & ZHANG, Y. 2021 Experimental investigation on the effect of particles on large scale vortices of an isolated hemispherical roughness element. *Phys. Fluids* **33** (6), 063308.

GRESHO, P.M. & SANI, R.L. 1987 On pressure boundary conditions for the incompressible Navier–Stokes equations. *Intl J. Numer. Meth. Fluids* **7** (10), 1111–1145.

GUALA, M., TOMKINS, C.D., CHRISTENSEN, K.T. & ADRIAN, R.J. 2012 Vortex organization in a turbulent boundary layer overlying sparse roughness elements. *J. Hydraul. Res.* **50** (5), 465–481.

GURKA, R., LIBERZON, A., HEFETZ, D., RUBINSTEIN, D. & SHAVIT, U. 1999 Computation of pressure distribution using PIV velocity data. In *3rd International Symposium on Particle Image Velocimetry – Santa Barbara,* pp. 1–6.

HAIDARI, A.H. & SMITH, C.R. 1994 The generation and regeneration of single hairpin vortices. *J. Fluid Mech.* **277**, 135–162.

HAJIMIRZAIE, S.M., WOJCIK, C.J. & BUCHHOLZ, J.H.J. 2012 The role of shape and relative submergence on the structure of wakes of low-aspect-ratio wall-mounted bodies. *Exp. Fluids* **53** (6), 1943–1962.

HE, G., WANG, J. & PAN, C. 2013 Initial growth of a disturbance in a boundary layer influenced by a circular cylinder wake. *J. Fluid Mech.* **718**, 116–130.

HINZE, J.O. 1975 *Turbulence*. McGraw-Hill.

VAN HOUT, R., EISMA, J., ELSINGA, G.E. & WESTERWEEL, J. 2018 Experimental study of the flow in the wake of a stationary sphere immersed in a turbulent boundary layer. *Phys. Rev. Fluids* **3** (2), 024601.

VAN HOUT, R., HERSHKOVITZ, A., ELSINGA, G.E. & WESTERWEEL, J. 2022 Combined three-dimensional flow field measurements and motion tracking of freely moving spheres in a turbulent boundary layer. *J. Fluid Mech.* **944**, A12.

JODAI, Y. & ELSINGA, G.E. 2016 Experimental observation of hairpin auto-generation events in a turbulent boundary layer. *J. Fluid Mech.* **795**, 611–633.

JOHNSON, K.C., THUROW, B.S., KIM, T., BLOIS, G. & CHRISTENSEN, K.T. 2017 Volumetric velocity measurements in the wake of a hemispherical roughness element. *AIAA J.* **55** (7), 2158–2173.

DE KAT, R. & GANAPATHISUBRAMANI, B. 2013 Pressure from particle image velocimetry for convective flows: a Taylor's hypothesis approach. *Meas. Sci. Technol.* **24**, 024002.

DE KAT, R. & VAN OUDHEUSDEN, B.W. 2012 Instantaneous planar pressure determination from PIV in turbulent flow. *Exp. Fluids* **52** (5), 1089–1106.

KIRIAKOS, R.M., RIVERO, M.J., POURNADALI KHAMSEH, A. & DEMAURO, E.P. 2021 Unsteady motion in the supersonic flow over a wall-mounted hemisphere. *AIAA J.* **60** (2), 688–698.

KLEBANOFF, P.S., CLEVELAND, W.G. & TIDSTROM, K.D. 1992 On the evolution of a turbulent boundary layer induced by a three-dimensional roughness element. *J. Fluid Mech.* **237**, 101–187.

KLEBANOFF, P.S., TIDSTROM, K.D. & SARGENT, L.M. 1962 The three-dimensional nature of boundary-layer instability. *J. Fluid Mech.* **12** (1), 1–34.

KOSCHATZKY, V., MOORE, P.D., WESTERWEEL, J., SCARANO, F. & BOERSMA, B.J. 2011 High speed PIV applied to aerodynamic noise investigation. *Exp. Fluids* **50** (4), 863–876.

KUNDU, P.K., COHEN, I.M. & DOWLING, D.R. 2015 *Fluid Mechanics*. Academic.

LI, J., QIU, X., SHAO, Y., LIU, H., FU, Y., TAO, Y. & LIU, Y. 2022 Turbulent coherent structures in channel flow with a wall-mounted hemisphere. *AIP Adv.* **12** (3), 035006.

LIU, X. & KATZ, J. 2006 Instantaneous pressure and material acceleration measurements using a four-exposure PIV system. *Exp. Fluids* **41** (2), 227.

LIU, X. & KATZ, J. 2013 Vortex-corner interactions in a cavity shear layer elucidated by time-resolved measurements of the pressure field. *J. Fluid Mech.* **728**, 417–457.

LOISEAU, J., ROBINET, J., CHERUBINI, S. & LERICHE, E. 2014 Investigation of the roughness-induced transition: global stability analyses and direct numerical simulations. *J. Fluid Mech.* **760**, 175–211.

LUMLEY, J.L. 1967 The structure of inhomogeneous turbulent flows. In *Atmospheric Turbulence and Radio Propagation* (ed. A.M. Yaglom & V.I. Tatarski), pp. 166–178. Nauka.

LYNCH, K. & SCARANO, F. 2013 A high-order time-accurate interrogation method for time-resolved PIV. *Meas. Sci. Technol.* **24** (3), 035305.

LYNCH, K.P. & SCARANO, F. 2015 An efficient and accurate approach to MTE-MART for time-resolved tomographic PIV. *Exp. Fluids* **56**, 1–16.

MANHART, M. 1998 Vortex shedding from a hemisphere in a turbulent boundary layer. *Theor. Comput. Fluid Dyn.* **12** (1), 1–28.

MOHAGHAR, M., ADHIKARI, D. & WEBSTER, D.R. 2019 Characteristics of swimming shelled Antarctic pteropods (*Limacina helicina antarctica*) at intermediate Reynolds number regime. *Phys. Rev. Fluids* **4** (11), 111101.

MORTAZAVI, M., KNIGHT, D.D., AZAROVA, O.A., SHI, J. & YAN, H. 2014 Numerical simulation of energy deposition in a supersonic flow past a hemisphere. In *52nd Aerospace Sciences Meeting*, p. 0944.

MURPHY, D.W., ADHIKARI, D., WEBSTER, D.R. & YEN, J. 2016 Underwater flight by the planktonic sea butterfly. *J. Expl Biol.* **219**, 535.

NOVARA, M. & SCARANO, F. 2012*a* Lagrangian acceleration evaluation for tomographic PIV: a particle-tracking based approach. In *Proceedings of the 16th International Symposium on Applications of Laser Techniques to Fluid Mechanics, Lisbon, Portugal*, pp. 9–12.

NOVARA, M. & SCARANO, F. 2012*b* Performances of motion tracking enhanced Tomo-PIV on turbulent shear flows. *Exp. Fluids* **52** (4), 1027–1041.

VAN OUDHEUSDEN, B.W. 2008 Principles and application of velocimetry-based planar pressure imaging in compressible flows with shocks. *Exp. Fluids* **45** (4), 657–674.

VAN OUDHEUSDEN, B.W. 2013 PIV-based pressure measurement. *Meas. Sci. Technol.* **24** (3), 032001.

VAN OUDHEUSDEN, B.W., SCARANO, F., ROOSENBOOM, E.W.M., CASIMIRI, E.W.F. & SOUVEREIN, L.J. 2007 Evaluation of integral forces and pressure fields from planar velocimetry data for incompressible and compressible flows. *Exp. Fluids* **43** (2–3), 153–162.

PAN, C., WANG, J., ZHANG, P. & FENG, L. 2008 Coherent structures in bypass transition induced by a cylinder wake. *J. Fluid Mech.* **603**, 367–389.

PREVEL, M., VINKOVIC, I., DOPPLER, D., PERA, C. & BUFFAT, M. 2013 Direct numerical simulation of particle transport by hairpin vortices in a laminar boundary layer. *Intl J. Heat Fluid Flow* **43**, 2–14.

PU, Y. & MENG, H. 2000 An advanced off-axis holographic particle image velocimetry (HPIV) system. *Exp. Fluids* **29** (2), 184–197.

QIN, Y. & MENG, W. 2009 Computational study of roughness-induced boundary-layer noise. *AIAA J.* **47** (10), 2417–2429.

RINOSHIKA, H., RINOSHIKA, A., WANG, J. & ZHENG, Y. 2021 3D flow structures behind a wall-mounted short cylinder. *Ocean Engng* **221**, 108535.

ROBINSON, S.K. 1991 Coherent motions in the turbulent boundary layer. *Annu. Rev. Fluid Mech.* **23**, 601–639.

SABATINO, D.R. & ROSSMANN, T. 2015 Tomographic PIV measurements of a regenerating hairpin vortex. *Exp. Fluids* **57**, 1–13.

SAVORY, E. & TOY, N. 1986*a* The flow regime in the turbulent near wake of a hemisphere. *Exp. Fluids* **4** (4), 181–188.

SAVORY, E. & TOY, N. 1986*b* Hemisphere and hemisphere-cylinders in turbulent boundary layers. *J. Wind Engng Ind. Aerodyn.* **23**, 345–364.

SCARANO, F. 2002 Iterative image deformation methods in PIV. *Meas. Sci. Technol.* **13** (1), R1–R19.

SCARANO, F. 2013 Tomographic PIV: principles and practice. *Meas. Sci. Technol.* **24** (1), 012001.

SCHRÖDER, A., GEISLER, R., ELSINGA, G.E., SCARANO, F. & DIERKSHEIDE, U. 2008 Investigation of a turbulent spot and a tripped turbulent boundary layer flow using time-resolved tomographic PIV. *Exp. Fluids* **44** (2), 305–316.

SIROVICH, L. 1987 Turbulence and the dynamics of coherent structures. I – coherent structures. II – symmetries and transformations. III – dynamics and scaling. *Q. Appl. Maths* **45**, 561–571.

SVIZHER, A. & COHEN, J. 2006*a* Holographic particle image velocimetry measurements of hairpin vortices in a subcritical air channel flow. *Phys. Fluids* **18** (1), 014105.

SVIZHER, A. & COHEN, J. 2006*b* Holographic particle image velocimetry system for measurements of hairpin vortices in air channel flow. *Exp. Fluids* **40**, 708–722.

TAMAI, N., ASAEDA, T. & TANAKA, N. 1987 Vortex structures around a hemispheric hump. *Boundary-Layer Meteorol.* **39** (3), 301–314.

TANG, Z. & JIANG, N. 2012 Dynamic mode decomposition of hairpin vortices generated by a hemisphere protuberance. *Sci. China Phys. Mech.* **55** (1), 118–124.

TANI, I. 1981 Three-dimensional aspects of boundary-layer transition. *Sadhana-Acad. P. Engng S.* **4** (2), 219.

TAVAKOL, M.M. & YAGHOUBI, M. 2010 Experimental and numerical analysis of turbulent air flow around a surface mounted hemisphere. *Sci. Iran.* **17** (6), 480.

TAVAKOL, M.M., YAGHOUBI, M. & MOTLAGH, M.M. 2010 Air flow aerodynamic on a wall-mounted hemisphere for various turbulent boundary layers. *Exp. Therm. Fluid Sci.* **34** (5), 538–553.

THEODORSEN, T. 1952 Mechanism of turbulence. In *Proceedings of the Second Midwestern Conference on Fluid Mechanics*, pp. 1–18. Ohio State University.

THOMAS, F.O. & LIU, X. 2004 An experimental investigation of symmetric and asymmetric turbulent wake development in pressure gradient. *Phys. Fluids* **16** (5), 1725–1745.

TOWNSEND, A.A. 1961 Equilibrium layers and wall turbulence. *J. Fluid Mech.* **11** (01), 97–120.

TOY, N., MOSS, W.D. & SAVORY, E. 1983 Wind tunnel studies on a dome in turbulent boundary layers. *J. Wind Engng Ind. Aerodyn.* **11** (1–3), 201–212.

TU, H., WANG, F., WANG, H., GAO, Q. & WEI, R. 2022 Experimental study on wake flows of a live fish with time-resolved tomographic PIV and pressure reconstruction. *Exp. Fluids* **63** (1), 1–12.

WANG, C., GAO, Q., WANG, J., WANG, B. & PAN, C. 2019 Experimental study on dominant vortex structures in near-wall region of turbulent boundary layer based on tomographic particle image velocimetry. *J. Fluid Mech.* **874**, 426–454.

WANG, C., GAO, Q., WANG, H., WEI, R., LI, T. & WANG, J. 2016*a* Divergence-free smoothing for volumetric PIV data. *Exp. Fluids* **57** (1), 15.

WANG, C., GAO, Q., WEI, R., LI, T. & WANG, J. 2016*b* 3D flow visualization and tomographic particle image velocimetry for vortex breakdown over a non-slender delta wing. *Exp. Fluids* **57** (6), 1–13.

WANG, C., GAO, Q., WEI, R., LI, T. & WANG, J. 2017*a* Spectral decomposition-based fast pressure integration algorithm. *Exp. Fluids* **58** (7), 84.

WANG, D., ZHAO, Y., XIA, Z., WANG, Q. & HUANG, L. 2012 Experimental investigation of supersonic flow over a hemisphere. *Chinese Sci. Bull.* **57** (15), 1765–1771.

WANG, H., GAO, Q., WANG, Z. & WANG, J. 2018 Error reduction for time-resolved PIV data based on Navier–Stokes equations. *Exp. Fluids* **59**, 149.

WANG, H., GAO, Q., WEI, R. & WANG, J. 2016*c* Intensity-enhanced MART for tomographic PIV. *Exp. Fluids* **57** (5), 87.

WANG, Y., HUANG, W. & XU, C. 2015 On hairpin vortex generation from near-wall streamwise vortices. *Acta Mechanica Sin.* **31** (2), 139–152.

WANG, Z., GAO, Q., PAN, C., FENG, L. & WANG, J. 2017*b* Imaginary particle tracking accelerometry based on time-resolved velocity fields. *Exp. Fluids* **58** (9), 113.

WANG, Z., GAO, Q., WANG, C., WEI, R. & WANG, J. 2016*d* An irrotation correction on pressure gradient and orthogonal-path integration for PIV-based pressure reconstruction. *Exp. Fluids* **57** (6), 104.

WIENEKE, B. 2008 Volume self-calibration for 3D particle image velocimetry. *Exp. Fluids* **45**, 549–556.

WOOD, J.N., DE NAYER, G., SCHMIDT, S. & BREUER, M. 2016 Experimental investigation and large-eddy simulation of the turbulent flow past a smooth and rigid hemisphere. *Flow Turbul. Combust.* **97** (1), 79–119.

YANG, W., MENG, H. & SHENG, J. 2001 Dynamics of hairpin vortices generated by a mixing tab in a channel flow. *Exp. Fluids* **30** (6), 705–722.

YE, Q., SCHRIJER, F. & SCARANO, F. 2016*a* Boundary layer transition mechanisms behind a micro-ramp. *J. Fluid Mech.* **793**, 132–161.

YE, Q., SCHRIJER, F. & SCARANO, F. 2016*b* Geometry effect of isolated roughness on boundary layer transition investigated by tomographic PIV. *Intl J. Heat Fluid Flow* **61**, 31–44.

YE, Q., SCHRIJER, F. & SCARANO, F. 2018 On Reynolds number dependence of micro-ramp-induced transition. *J. Fluid Mech.* **837**, 597–626.

YE, Z., GAO, Q., WANG, H., WEI, R. & WANG, J. 2015 Dual-basis reconstruction techniques for tomographic PIV. *Sci. China Technol. Sci.* **58** (9), 1–8.

ZHANG, X., TUNA, B.A., YARUSEVYCH, S. & PETERSON, S.D. 2021 Flow development over isolated droplet-inspired shapes. *Intl J. Heat Fluid Flow* **88**, 108756.

ZHOU, J., ADRIAN, R.J., BALACHANDAR, S. & KENDALL, T.M. 1999 Mechanisms for generating coherent packets of hairpin vortices in channel flow. *J. Fluid Mech.* **387**, 353–396.

ZHU, H., WANG, C., WANG, H. & WANG, J. 2017 Tomographic PIV investigation on 3D wake structures for flow over a wall-mounted short cylinder. *J. Fluid Mech.* **831**, 743–778.